TRIBHUVAN UNIVERSITY
INSTITUTE OF ENGINEERING
PULCHOWK CAMPUS

B-11-BAS-2019/24

NUMERICAL SIMULATION OF HYPERSONIC FLUID-STRUCTURE INTERACTION ON CANTILEVER PLATE WITH OSCILLATING SHOCK IMPINGEMENT

By:
Prabin Paudel (076BAS026)
Sanskar Chandra Shahi (076BAS037)
Sarthak Pandey (076BAS039)
Sashakta Kharel (076BAS040)

A PROJECT REPORT SUBMITTED TO THE DEPARTMENT OF MECHANICAL AND AEROSPACE ENGINEERING IN PARTIAL FULFILLMENT OF THE REQUIREMENT FOR THE BACHELOR'S DEGREE IN AEROSPACE ENGINEERING

DEPARTMENT OF MECHANICAL AND AEROSPACE ENGINEERING
LALITPUR, NEPAL

March, 2024

COPYRIGHT

Head of Department
Department of Mechanical and Aerospace Engineering,
Institute of Engineering, Pulchowk Campus,
Lalitpur, Nepal

TRIBHUVAN UNIVERSITY
INSTITUTE OF ENGINEERING
PULCHOWK CAMPUS
DEPARTMENT OF MECHANICAL AND AEROSPACE ENGINEERING

LETTER OF APPROVAL

The undersigned certify that they have read, and recommended to the Institute of Engineering for acceptance, a project report entitled **"Numerical Simulation of Hypersonic Fluid-Structure Interaction on Cantilever Plate with Oscillating Shock Impingement"** submitted by **Prabin Paudel, Sanskar Chandra Shahi, Sarthak Pandey and Sashakta Kharel** in partial fulfilment of the requirements for the Bachelor's Degree in Aerospace Engineering.

Supervisor: **Sudip Bhattarai (PhD)**
Assistant Professor
Department of Mechanical and Aerospace Engineering
Institute of Engineering, Pulchowk Campus

External Examiner: **Er. Sanjiv Paudel**
Managing Director
Machine Hub Nepal

Head of Department: **Sudip Bhattarai (PhD)**
Assistant Professor
Department of Mechanical and Aerospace Engineering
Institute of Engineering, Pulchowk Campus

DATE OF APPROVAL: March 13, 2024

ABSTRACT

When an entity surpasses the velocity of sound, it undergoes a process where it compresses the air molecules preceding it, resulting in the formation of a region characterized by heightened pressure called a shock wave. When this shock wave encounters a physical framework, the framework becomes exposed to a load of pressure, potentially leading to structural deformation. These scenarios, wherein the interaction between a fluid medium and structures is involved, are effectively tackled through the discipline of fluid-structure interaction (FSI). In the case of hypersonic vehicles, shock waves impact the structures of control surfaces, thereby instigating fluid-structure interaction within said structures. The scope of this study is to carry out a numerical simulation of Hypersonic Fluid-Structure Interaction on a Cantilever plate with oscillating shock impingement location using the UNSW Canberra's HyMAX benchmark test case. The numerical simulation is carried out in two approaches i.e. Low Fidelity Modeling (LFM) and High Fidelity Modeling (HFM). In LFM, the problem is modeled based on shockwave Expansion Theory , Piston Theory and Euler Bernoulli Model. Whereas in HFM, the problem is solved by coupling a fluid solver, OpenFOAM, with a structural solver, CalculiX, via a coupling library, preCICE. The shock-generating wedge was given a predefined oscillating rotating motion with a frequency of 42 Hz. Subsequently, with inviscid and viscous FSI, a power spectral density plot of the trailing edge displacement profile shows two dominant peaks at 42 Hz and 90 Hz, which matches the experimental results. The power spectra of peak pressure evolution at the cantilever plate show a dominant spectral peak at 42 Hz and a second peak at 85 Hz. The trailing edge displacement obtained on the first cycle was 3.15 mm from viscous simulations and 3.01 mm from inviscid simulations, with an error of 1.86 % and 6.2 %, respectively. The PSD of trailing edge displacement via LFM shows the spectral peak at 42 Hz and 92.7 Hz (an error of 3%).

Keywords: *aeroelasticity, fluid-structure interaction, shockwave boundary layer interaction, oscillating shock impingement, numerical schlieren, separation bubble dynamics*

ACKNOWLEDGEMENT

Foremost, we would like to express our sincere appreciation to Dr. Sudip Bhattarai, our project supervisor and Yoda to our Luke Skywalker for his consistent guidance and invaluable encouragement. We genuinely acknowledge his invaluable supervision and insightful suggestions. We would also like to acknowledge the original work of Dr. Gaetano Currao in formulating the HyMAX concept and the experimental work of Dr. Tallaru Murali Krishna, upon which this numerical study is based. Their work was the wind beneath our project's wings.

We extend our gratitude to the Department of Mechanical and Aerospace Engineering at the Institute of Engineering, Pulchowk Campus, for providing us with the opportunity to engage in this collaborative endeavour. This opportunity has allowed us to apply the knowledge we have acquired throughout our years of study as a major project in our fourth year. Developing our own major project has significantly enriched our knowledge and provided us with a valuable experience in teamwork.

We would like to express our sincere gratitude to Er. Nishchal Poudel, Er. Sambhav Sahani and Er. Subarna Pudasaini for their unwavering support and extensive guidance. We would also like to thank Er. Anup Pandey, Er. Sandip Gyawali and Er. Bibek Adhikari, our lighthouses in the stormy sea of this project, for providing us technical enlightenment during our dark days.

We also extend our thanks to all of our friends who have directly or indirectly supported us in completing this project. You guys were the Samwise to our Frodo. Lastly, we hold a deep appreciation for our family members who have consistently served as a source of inspiration for us.

We welcome and greatly value any suggestions or criticisms that may contribute to the improvement of this project, and we sincerely acknowledge them.

Authors:
Prabin Paudel (076BAS026)
Sanskar Chandra Shahi (076BAS037)
Sarthak Pandey (076BAS039)
Sashakta Kharel (076BAS040)

TABLE OF CONTENTS

List of Figures

List of Tables

LIST OF ABBREVIATIONS

2D	Two Dimensional
3D	Three Dimensional
AePW3	Aeroelastic Prediction Workshop 3
CFD	Computational Fluid Dynamics
FEA	Finite Element Analysis
FEM	Finite Element Method
FSI	Fluid-Structure Interaction
GAMG	Geometric Agglomerated Algebraic Multigrid
GCI	Grid Convergence Index
HFM	High Fidelity Method
HyMAX	Hypersonic Multibody Aeroelastic eXperiment
LFM	Low Fidelity Method
NI	Newtonian Impact
NS	Navier-Stokes
OpenFOAM	Open-source Field Operation and Manipulation
PSD	Power Spectral Density
PT	Piston Theory
PreCICE	Precise Code Interaction Coupling Environment
RANS	Reynolds-Averaged Navier Stokes
SE	Shock-Expansion
SWBLI	Shock-Wave Boundary Layer Interaction
TE	Trailing Edge
UNSW	University of New South Wales

LIST OF SYMBOLS

p	Pressure
γ	Gas Constant
M	Mach Number
θ	Local Deflection Angle
ρ	Density of Air
e	Specific Energy
u	Velocity
τ	Shear Stress
T	Static Temperature
k	Conductivity
μ	Viscosity Coefficient
C_p	Specific Heat Capacity at Constant Pressure
C_v	Specific Heat Capacity at Constant Volume
R	Specific Gas Constant
Pr	Prandtl Number
w	Plate Deflection
D	Flexural Rigidity
E	Youngs's Modulus
I	Moment of Inertia
μ_m	Mass Per Unit Length
h	Thickness of Plate
L	Length of the Plate
l	Length of an Element
σ	Stress
B	Body Force
M	Elemental Mass Matrix
K	Elemental Stiffness Matrix
$\bar{D}$	Elemental Damping Matrix
α,β	Rayleigh Damping Coefficients
ζ_1, ζ_2	Damping Ratios
∞	Freestream
loc	Local
pk	peak

CHAPTER 1: INTRODUCTION

1.1. Background

The shock wave is a type of propagating disturbance that carries energy, momentum, and information through a fluid medium. It is characterized by a sudden and rapid increase in density, temperature and pressure as it moves through the medium. When an object moves faster than the speed of sound, it compresses the air molecules in front of it, creating a high-pressure region which is known as a shock wave. When the shock wave impinges on a structure, the structure is subjected to pressure load, which can cause the structure to deform. Such problems where fluid medium and structures interact are addressed by fluid-structure interaction (FSI). Fluid-structure interaction (FSI) is a multi physics coupling between the laws that describe fluid dynamics and structural mechanics. The behavior of the flow is influenced by the form and movement of the structure, while the movement and deflection of the structure are dictated by the aerodynamic forces acting on it [2].

Figure 1.1: X-15A-2, sky blue circle indicates the speed brake
[3]

FSI, or Fluid-Structure Interactions, are commonly found in engineering challenges. Therefore, techniques that can forecast these interactions are highly sought after in various fields such as the aerospace industry, research labs, medical sectors, and many other areas. Some applications of FSI may include but not limited to fluttering of wings, deflection of wing on aerodynamic loading, energy harvesting from fluid flow.

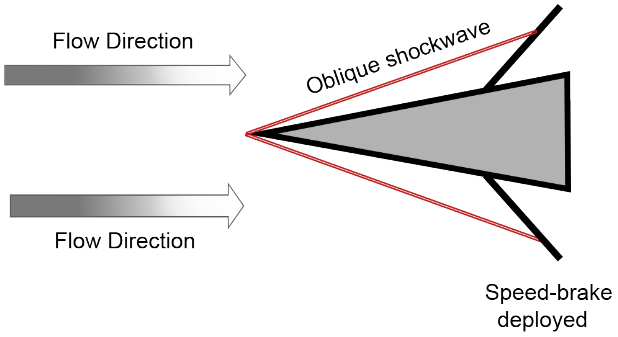

Figure 1.2: Flow over vertical stabilizer
[4]

In hypersonic vehicles, shock waves impinge on the control surface structures and hence fluid-structure interaction occurs on such structures. University of New South Wales (UNSW) Canberra hypersonic experiment has been established as a benchmark test demonstrating fluid-structure interaction in hypersonic flow (AePW3 - High Speed Working Group). During flight maneuvers, shockwaves of various intensities can impinge on different locations of the control surface, fuselage, engine cowl etc. In scramjet engine, shockwaves of varying intensity can form in intake region. Similar phenomenon can be seen in vertical stabilizer of X-15A-2. The shockwave formed at the leading edge of the vertical stabilizer may impinge on the aerobrake surface causing overheating issues, as shown in figure 1.1. Similarly, the compression corner formed at the hinge of the aerobrake presents a physics similar to that of shockwave impingement [4].

Shockwave impinging on surface results in shock wave boundary layer interaction which affects the flow properties within the boundary layer. The shockwave increases the pressure and temperature abruptly, leading to a significant change in flow characteristics. When shockwave impinges on boundary layer, it creates adverse pressure gradient. This interaction can cause flow separation locally, where the boundary layer separates from the surface, leading to a change in aerodynamic forces and creates a separation bubble. SWBLI can result in high thermal loads in structure which may result in the structure to exhibit aerothermoelastic behavior [5]. Such problems are more complex and do not lie within the domain of this study. Due to the above mentioned reasons, the study of FSI is essential in the field of hypersonic.

1.2. Problem Statement

This study is a direct continuation of work carried out by Dr. Gaetano M. Currao *et. al.*[6], Dr. Murali Krishna Talluru *et. al.*[7] and Mr. Nischal Poudel, Mr. Sambhav Sahani and Mr. Subarna Pudasaini [1]. Complex FSI problems encountered in hypersonic flow are next to impossible to solve analytically. The experimental setup for carrying out the test is expensive and not feasible under every circumstance. We can solve the FSI problems numerically to demonstrate how the impinging shockwave affects the structure. By oscillating the shock generator, we can demonstrate how impinging shockwave in different locations at different rates affects the structure. Taking the UNSW Canberra's HyMAX benchmark test case as reference, we want to solve the problem numerically and compare with the results obtained experimentally in [7] and determine the effectiveness of solving the problem numerically. When the shock generator oscillates, oblique shock impingement location changes as shown in figure 1.3 and figure 1.4. The intensity of impinging shock also varies as the shock generator oscillates from -5° to 5°. We can solve the problem analytically using Low Fidelity Modeling (LFM) and numerically using High Fidelity Modeling (HFM) based on our requirement of accuracy and computational efficiency. High Fidelity Modeling can generate accurate results at the expense of expensive computational costs. Whereas Low Fidelity Modeling may not be able to predict the problem accurately but uses less computational resources and time. So, we need to determine a procedure to predict the result within allowable error ε and minimizing computational cost as much as feasible.

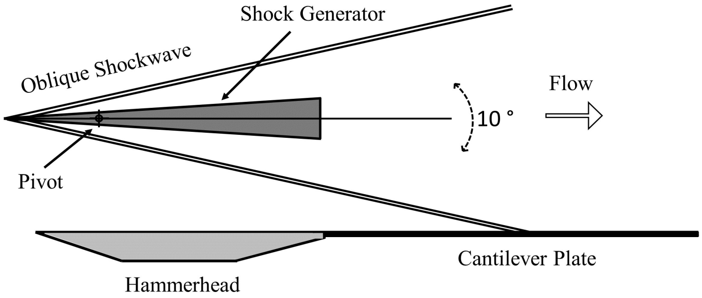

Figure 1.3: Oblique Shockwave at Mean Position of Shockwave Generator

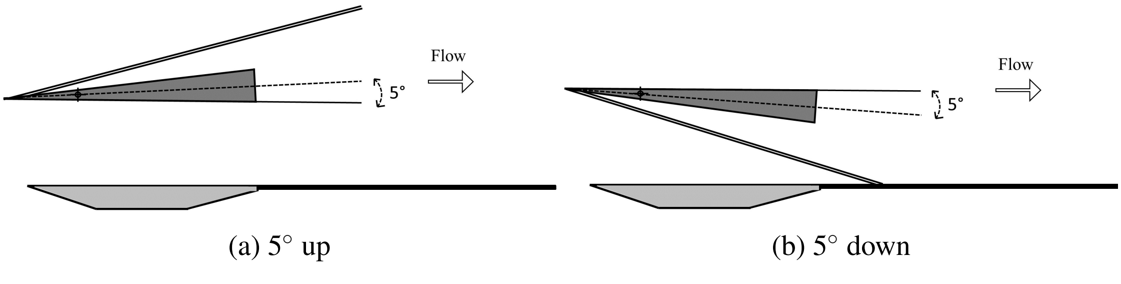

(a) 5° up

(b) 5° down

Figure 1.4: Shockwave at Max Limits of Shockwave Generator

1.3. Objectives

1.3.1. Main Objective

The main objective of this study is to carry out a numerical simulation of hypersonic fluid-structure interaction on a cantilever plate with oscillating shock impingement.

1.3.2. Specific Objectives

- To model the problem (HyMAX) using high-fidelity and low-fidelity methods.
- Investigate how the SWBLI occurs when oscillating shock impinges on a cantilever plate.
- Verify the results obtained by comparing them with experimental results obtained by [7].

1.4. System Requirements

1.4.1. Hardware Requirements

A computer with the following specifications was used:

- 16 cores CPU
- 32 GB RAM
- 512 GB SSD

1.4.2. Software Requirements

Softwares used in the duration of this work are:

- OpenFOAM: It is used to solve the fluid domain.
- CalculiX: It is used to solve the solid domain.
- preCICE: It is used for coupling the fluid and structural domain.
- PrePoMax: It is used for mesh generation for the solid domain.
- MATLAB: It is used to develop the low fidelity model.
- ParaView: It is used to post process the results.
- Inkscape: It is used for the preparation and layout of figures.

CHAPTER 2: LITERATURE REVIEW

First hypersonic flight can be recorded back to 1949 when WAC Corporal, a second stage rocket of V2, became first man made object to achieve hypersonic flight [8]. Since then numerous hypersonic flight were recorded. With the advent of hypersonic flights, numerous studies on high-speed aeroelasticity have been conducted. First documented evidence of high speed aeroelastic study can be dated back to mid 1950's [4]. Early experiment works included study on structural instabilities of whole vehicle or components, such as wing or control surface, undergoing high speed flights. Behaviour of fundamental shapes such as rigid plates and wedge on high speed flow were also studied. The main objective of experimental study was to compare the theoretical result with experimental result and to establish the boundary of Mach number where whole vehicle or its individual component would face instability issues such as fluttering [4].

The discipline of hypersonic FSI combines principles from fluid dynamics, structural mechanics, and heat transfer to model and simulate the interaction between the fluid flow and solid structures. It takes into account factors such as shock waves, boundary layer interactions, thermal effects, and structural deformation under extreme conditions. Aeroelastic simulations are especially important in the hypersonic regime since the traditional method of testing using aero-elastically scaled wind tunnel models is impractical as in subsonic and supersonic flows [9]. Since laboratory experiments are constrained in scope and analytical solutions to the model equations are normally not possible for most FSI problems, numerical simulations must be employed to examine the underlying physics of the complicated interaction between fluids and solids [10].

Since it is essential to comprehend SWBLI and its implications for the development of hypersonic vehicles, SWBLI has been the subject of various research for many years. One such consequence is the localized aerodynamic heating, which gets worse as the Mach number rises [8]. In [11], the interaction of an external oblique shock with the turbulent boundary layer atop the flat plate and viscous interactions in a 2-D compression corner have been studied experimentally. These interactions were studied at freestream Mach number ranging from 6.5 to 13 , Re ranging from $1x10^7$ to $1x10^8$ and wall-to-freestream stagnation temperature ratios ranging from 0.1 to 0.4. It was found that with increase in Re, there was an increase in the length of separation region, an increase in wall-to-freestream stagnation temperature ratio and a decrease in freestream Mach number.

In [4], SWBLI on a rigid plate was observed experimentally. It was found that when an oblique shock impinged on the boundary layer, the boundary layer separated upstream of the impingement location and reattached downstream of the flow. It was observed that Görtler vortices were formed which was attributed as the cause of boundary layer instability. This instability, in turn, caused the transition of boundary layer, which took place within the separation region. Thus near the reattachment point, boundary layer can be considered turbulent. In [12], it was shown that an eigenvalue problem resulted from the interaction of an oscillating shock with a laminar boundary layer. For specific values of shock strength and frequency, self-supported oscillations of the flow pattern occur. This mechanism or a similar mechanism involving a turbulent boundary layer could contribute to the initiation of transonic buzz and buffeting.

In [13], two primary modes of low-frequency fluctuations were recognized: the first includes an upstream mechanism, where there is unsteadiness due to upstream disturbances; the second includes a downstream mechanism, where the bubble's dynamics are linked to motion of the shock. Compared to the unsteadiness associated with SWBLIs, there is considerably less focus on the unsteadiness induced by the motion of the shock generator. As noted previously, such conditions may be due to vehicle maneuvers, control surface modulation, or aeroelastic behavior. These would typically occur at lower frequencies than unsteadiness induced by SWBLIs, specifically, 0-100 Hz. Previously, numerical and experimental studies have been done [14], with oscillating shock impingement on flat plate but there is a lack of research on oscillating shock impingement on complaint plates in a hypersonic regime.

For the preliminary design and sensitivity analysis of hypersonic configurations, a number of approximate unsteady aerodynamic theories are used that assume inviscid flow and ignore real gas effects, including the Piston Theory (PT), Van Dyke's second-order theory, Newtonian Impact (NI) theory, and unsteady Shock-Expansion (SE) theory [15].

High-fidelity modelling of hypersonic FSI presents a substantial challenge, extending beyond computational expenses. The primary challenge lies in ensuring the FSI coupling meets the criteria of both accuracy and stability throughout the time evolution of the solution. This complexity arises from the fact that fluid governing equations are formulated in the Eulerian frame of reference, while structural governing equations are expressed in the Lagrangian frame of reference. Integrating these two frames poses a challenge due to their inherent differences.

In [15], authors examined various low fidelity approximation theories by comparing them with predictions from high fidelity CFD solutions to unsteady NS equations. A substitute model based on combined steady state computational fluid dynamics and piston theory was assessed and can be used as an alternative to the time accurate Navier-Stokes solution.

Recent literatures are mainly focused on analytical, experimental, and computational predictions of FSI on the scramjet inlet as well as wings and control surfaces. All three approaches are being used, and the focus is to get agreement between them. In [16] the authors experimentally investigated the effect of FSI on the control authority of a trailing-edge flap through the hypersonic ground test of the rigid flap and compliant flap (of 1 mm thickness) at discrete angles of inclination and made a comparison with analytical and numerical predictions. High-fidelity numerical simulations have become much more common and accessible now with advancements in the computational field. However, experiments are limited to validate the results.

Efforts have been made at UNSW to produce fundamental FSI experiments using a shock generator and an oscillating plate [4, 17, 18]. In [6], authors discuss the design, measurement and simulation of an experiment in a Mach 6 wind tunnel where they conducted a study of static shock impingement on a cantilever plate and oscillating shock impingement on a rigid flat plate. Shock impingement point and shock-strength varied with a frequency of 42 Hz to resemble hypersonic vehicle components natural frequencies. In [7], authors performed experiments constituting of an oscillating shock impingement on the cantilever plate to understand the coupling between the moving shock dynamics and the compliance of the cantilever plate as it is subjected to fluid-structure interaction.

2.1. Research Gap

There is a lack of study on how to reconcile test and analysis in hypersonic FSI issues. It is necessary to do research on both the measurements that should be made in upcoming experiments in order to improve the test-analysis agreement and the best possible numerical analysis-experiment agreement. The latter research gap is the main focus of our study.

CHAPTER 3: THEORY

3.1. Hypersonic Flows

The definition of hypersonic flow may differ from person to person but as a rule of thumb, when free stream mach number is greater than 5, the flow is considered to be hypersonic flow. The hypersonic regime differs from supersonic regime as in hypersonic regime, flow is affected by phenomena such as thin shock layer, entropy layer, viscous interaction and gas dissosciation due to high gas temperature. [8].

3.2. Shock-Wave Boundary Layer Interaction (SWBLI)

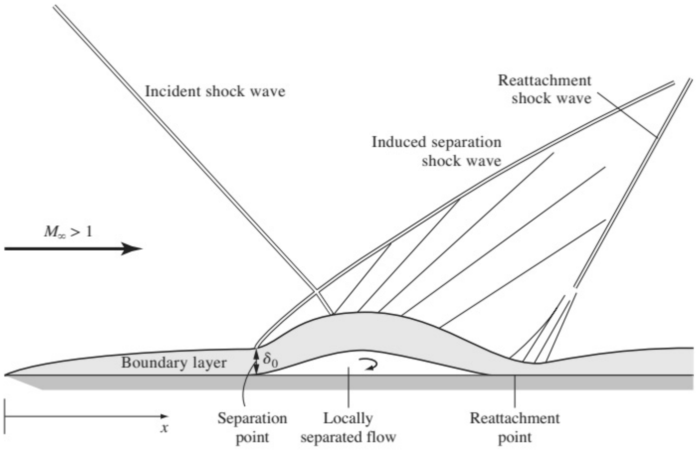

Figure 3.1: Schematic of shock wave boundary layer interaction [19]

Shock wave can react with boundary layer in viscous flow causing multiple shocks. When a shock impinges on a surface, it creates adverse pressure gradient along the flow direction causing flow separation. The separated flow induces a separation shock wave as it bends the incoming flow towards itself. Similarly downstream when flow is attached, another shock is formed known as reattachment shock as the flow gets deflected towards itself. In the region between separation and attachment region, numerous compression waves are formed as flow gets deflected away from itself as shown in figure 3.1. Also the shock impingement point in inviscid flow differs from that in viscous flow in account to SWBLI. SWBLI can effect pressure distribution, shear stress distribution and heat transfer mechanism in hypersonic flows.

3.3. Shock-Expansion Theory

Shock expansion theory is a local surface inclination method used to calculate the flow properties such as flow Mach number and pressure behind shock waves and expansion waves. The mathematical equations for calculation of flow properties behind shock wave can be summarized as follows:

$$tan\theta = 2cot\beta \frac{M_1^2 sin\beta^2 - 1}{M_1^2(\gamma + cos2\beta) + 2} \tag{3.1}$$

$$\frac{P_2}{P_1} = 1 + \frac{2\gamma}{\gamma+1}\left(M_{n,1}^2 - 1\right) \tag{3.2}$$

$$M_{n,2}^2 = \frac{1 + [(\gamma-1)/2]M_{n,1}^2}{\gamma M_{n,1}^2 - (\gamma-1)/2} \tag{3.3}$$

Where '1' denotes the region before the shock wave and '2' denotes the region after the shock wave. 'n' in the subscript denotes the normal component of velocity component given by:

$$M_{n,1} = M_1 sin\beta \tag{3.4}$$

$$M_2 = \frac{M_{n,2}}{\sin(\beta - \theta)} \tag{3.5}$$

Where θ is the flow deflection angle and β is the angle made by shock wave with initial flow direction.

The mathematical equations for calculation of flow properties behind expansion fan can be summarized as follows:

$$\nu(M) = \sqrt{\frac{\gamma+1}{\gamma-1}} \tan^{-1}\left(\sqrt{\frac{\gamma-1}{\gamma+1}(M^2-1)}\right) - \tan^{-1}\left(\sqrt{M^2-1}\right) \tag{3.6}$$

where ν is defined as Pandtl-Meyer function.

$$\theta = \nu(M_2) - \nu(M_1) \tag{3.7}$$

where θ is the flow deflection angle.

As the expansion wave is considered to be isentropic process, we can use isentropic relations to calculate the flow properties:

$$p_{01} = p_{02} \tag{3.8}$$

$$\frac{p_0}{p} = \left(1 + \frac{\gamma - 1}{2} M^2\right)^{\frac{\gamma}{\gamma - 1}} \tag{3.9}$$

$$\frac{T_0}{T} = \left(1 + \frac{\gamma - 1}{2} M^2\right) \tag{3.10}$$

3.4. Piston Theory

Piston theory is used to estimate the pressure on surface structure when it undergoes deformation. The pressure on the surface of the structure is calculated using piston analogy in which a piston is assumed to move in a one dimension channel. The air molecules above the surface is assumed to compress isentropically by piston which is moving at velocity equal to that of structure plus free stream velocity times inclination angle as shown in figure 3.2. [4].

3.4.1. Classical Piston Theory

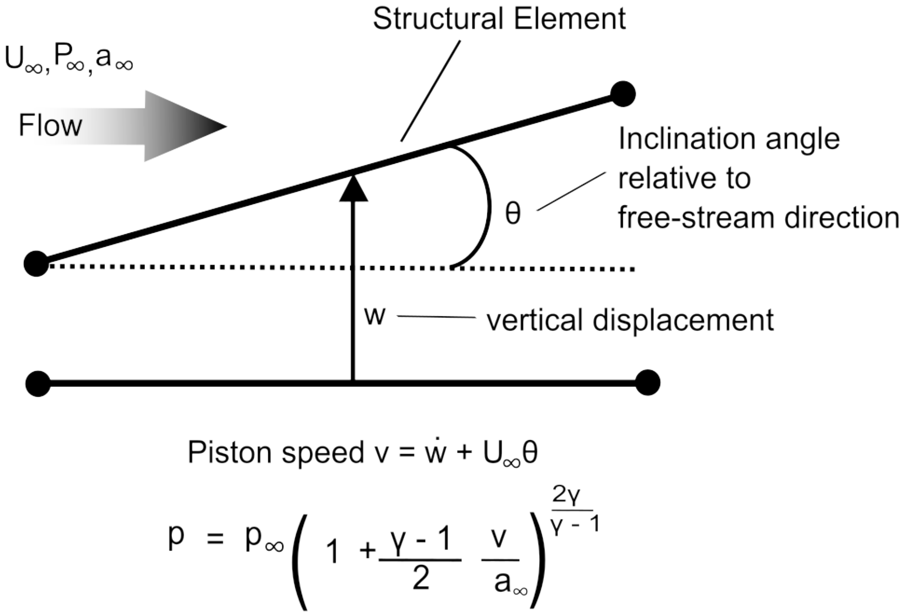

Figure 3.2: Piston theory representation

The local pressure is approximated using freestream flow quantities (pressure and Mach number).

Second order piston theory is given by:

$$p(x,t) = p_\infty(1 + \frac{\gamma - 1}{2} M_\infty \theta(t))^{\frac{2\gamma}{\gamma-1}} \tag{3.11}$$

Where $\dot{w}$ is ignored because it is very small compared to the free stream velocity, U_∞. Similarly, third order piston theory is given by:

$$p(x,t) = p_\infty(1 + \gamma M_\infty \theta(t) + \gamma \frac{\gamma - 1}{4} (M_\infty \theta(t))^2 + \gamma \frac{\gamma - 1}{4} (M_\infty \theta(t))^3) \tag{3.12}$$

3.4.2. Local Piston Theory

When the flow is three-dimensional and/or mach number and surface inclinations are high, the local pressure is approximated using the flow quantities as:
Second order:

$$p(x,t) = p_{loc}(1 + \frac{\gamma - 1}{2} M_{loc} \theta(t))^{\frac{2\gamma}{\gamma-1}} \tag{3.13}$$

Third order:

$$p(x,t) = p_{loc}(1 + \gamma M_l oc \theta(t) + \gamma \frac{\gamma - 1}{4} (M_{loc} \theta(t))^2 + \gamma \frac{\gamma - 1}{4} (M_{loc} \theta(t))^3) \tag{3.14}$$

3.4.3. CFD enriched Piston Theory

In this method, the flow quantities are extracted from steady state CFD results and fed into the piston theory fomulation to improve the approximations. For transient phenomenon such as oscillating shock waves, numerical errors may arise due to transient nature.

3.5. Governing Equations

3.5.1. Fluid

The governing Navier-Stokes (NS) equations, for 2-dimensional compressible, viscous flow, in indices form is given by:

$$\frac{\partial \rho}{\partial t} + \frac{\partial \rho u_i}{\partial x_i} = 0 \tag{3.15}$$

$$\frac{D\rho u_i}{Dt} = -\frac{\partial p}{\partial x_i} + \frac{\partial \tau_{ij}}{\partial x_i} \tag{3.16}$$

$$\frac{D\rho e}{Dt} = -p\frac{\partial u_i}{\partial x_i} + \tau_{ij}\frac{\partial u_i}{\partial x_j} + \frac{\partial (k\frac{\partial T}{\partial x_i})}{\partial x_i} \tag{3.17}$$

Where τ_{ij} denotes the viscous force term given by:

$$\tau_{ij} = \mu(\frac{\partial u_i}{\partial x_j} + \frac{\partial u_i}{\partial x_i} - \frac{2}{3}\frac{\partial u_k}{\partial x_k}\delta_{ij}) \tag{3.18}$$

The symbol D/Dt represents the substantial derivative given by:

$$\frac{D}{Dt} = \frac{\partial}{\partial t} + u_i\frac{\partial}{\partial x_j} \tag{3.19}$$

The indices represent the 2 orthogonal directions. So that:

$$\begin{aligned} i &= 1,2 \\ j &= 1,2 \\ k &= 1,2 \end{aligned} \tag{3.20}$$

$$\delta_{ij} = \begin{cases} 1 & \text{if } i = j \\ 0 & \text{if } i \neq j \end{cases} \tag{3.21}$$

Assuming the gas to be calorically perfect (for low freestream enthalpy, chemical aspects can be neglected):

$$\gamma = \frac{C_p}{C_v} \tag{3.22}$$

$$C_p - C_v = R \tag{3.23}$$

$$e = C_v T + \frac{u_i u_j}{2} \tag{3.24}$$

$$p = \rho R T \tag{3.25}$$

Where $\gamma = 1.4$ and $R = 287.05\,\mathrm{J\,kg^{-1}\,K^{-1}}$. The viscosity μ is calculated using the Sutherland relation:

$$\frac{\mu}{\mu_{ref}} = (\frac{T}{T_{ref}})^{\frac{3}{2}} \, \frac{T_{ref} + S}{T + S} \tag{3.26}$$

where $\mu_{\mathrm{ref}} = 1.789 \times 10^{-5}\,\mathrm{kg\,m^{-1}\,s^{-1}}$, $T_{\mathrm{ref}} = 288\,\mathrm{K}$, and S = 110 K. The thermal conductivity is defined as:

$$k = \frac{\mu C_p}{Pr} \tag{3.27}$$

The unsteady aerodynamic pressure is approximated using local piston theory as stated in equation (1.12) and (1.13).

3.5.2. Structure

The general form of the equations of motion for a deformable body [20] are:

$$\frac{\partial \sigma_{xx}}{\partial x} + \frac{\partial \sigma_{yx}}{\partial y} + \frac{\partial \sigma_{zx}}{\partial z} + B_x = 0 \tag{3.28}$$

$$\frac{\partial \sigma_{xy}}{\partial x} + \frac{\partial \sigma_{yy}}{\partial y} + \frac{\partial \sigma_{yz}}{\partial z} + B_y = 0 \tag{3.29}$$

$$\frac{\partial \sigma_{xz}}{\partial x} + \frac{\partial \sigma_{yz}}{\partial y} + \frac{\partial \sigma_{zz}}{\partial z} + B_z = 0 \tag{3.30}$$

The Euler-Bernoulli beam model equation which will be used in the 2D modeling of the plate for the low-fidelity method is:

$$D \frac{\partial^4 w}{\partial x^4} = p(x,t) - \mu_m \frac{\partial^2 w}{\partial t^2} \tag{3.31}$$

Where $D = \frac{EI}{1-v^2}$ is the flexural rigidity, μ_m is the mass per unit length and p is the net aerodynamic pressure acting on the structural element.

For a single beam element, the Finite Element Method (FEM) equation can be written as:

$$M\ddot{w} + \overline{D}\dot{w} + Kw = f \tag{3.32}$$

with:

$$M = \frac{\rho hl}{420}\begin{bmatrix} 156 & 22l & 54 & -13l \\ 22l & 4l^2 & 13l & -3l^2 \\ 54 & 13l & 156 & -22l \\ -13l & -3l^2 & -22l & 4l^2 \end{bmatrix} \tag{3.33}$$

$$K = \frac{D}{l^3}\begin{bmatrix} 12 & 6l & -12 & 6l \\ 6l & 4l^2 & -6l & 2l^2 \\ -12 & -6l & 12 & -6l \\ 6l & -2l^2 & -6l & 4l^2 \end{bmatrix} \tag{3.34}$$

$$f = \frac{l}{2}p(x,t)\begin{pmatrix} 1 \\ l/6 \\ 1 \\ -l/6 \end{pmatrix} \tag{3.35}$$

$$\overline{D} = \alpha M + \beta K \tag{3.36}$$

Where, f is the aerodynamic load, $\overline{D}$ is the damping matrix. M is the mass matrix and K is the stiffness matrix.

The stiffness damping coefficients α and β (for Rayleigh damping) are obtained given the first two natural frequencies and damping ratio:

$$\alpha = 2\omega_1\omega_2\frac{\zeta_1\omega_2 - \zeta_2\omega_1}{\omega_2^2 - \omega_1^2} \tag{3.37}$$

$$\beta = 2\frac{\zeta_2\omega_2 - \zeta_1\omega_1}{\omega_2^2 - \omega_1^2} \tag{3.38}$$

with,

$$\zeta_1 = \zeta_2 = \zeta \tag{3.39}$$

3.5.2.1 Modal Analysis

The natural frequency of a structure is related to the eigenvalues and eigenvectors of the mass and stiffness matrices. An eigenvalue is a scalar that indicates the magnitude of the vibration, while an eigenvector is a vector that indicates the shape of the vibration.

The eigenvalue problem is a mathematical equation that relates the mass and stiffness matrices to the eigenvalues and eigenvectors. The equation is:

$$Kx = \lambda Mx \tag{3.40}$$

where K is the stiffness matrix, M is the mass matrix, x is the eigenvector, and λ is the eigenvalue. The natural frequency is the square root of the eigenvalue multiplied by 2π. The equation can be rewritten as:

$$f = (1/2\pi)\sqrt{\lambda} \tag{3.41}$$

where f is the natural frequency.

3.5.3. FSI Interface

The interface region is of great importance as it separates both the fluid and structure domains. Data transfer between fluid and solid solutions also takes place through this region. For this, two sets of coupling conditions are specified as: kinematic and dynamic coupling conditions [21]. The kinematic coupling condition ensures that the fluid and structure have the same velocity and displacement at the interface.

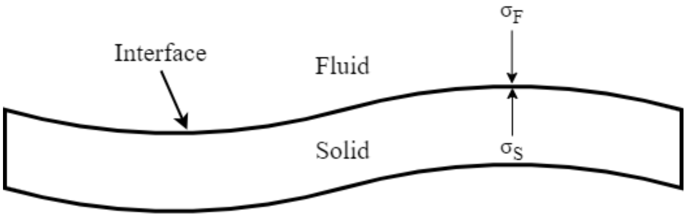

Figure 3.3: Fluid solid interface

$$x_F = w_S \tag{3.42}$$

$$v_F = \frac{\partial w_s}{\partial t} \tag{3.43}$$

Similarly, the dynamic coupling condition ensures the stress or force balance between the fluid and structure.

$$\sigma_F . n_F = -\sigma_S . n_S \tag{3.44}$$

3.6. FSI Coupling

3.6.1. Monolithic and Partitioned Approach

The simultaneous solution of governing equations for fluid, structure, and interface coupling conditions is achieved through a unified set of discretized equations in the monolithic approach. This method necessitates the use of a dedicated FSI solver. The FSI solution in the monolithic approach is regarded as precise, with any errors arising solely from the numerical scheme employed in the discretization process. Nonetheless, creating a monolithic approach from the ground up can be challenging in terms of coding. The partitioned approach employs distinct solvers for fluid and structure, utilizing a coupling application to address interface coupling conditions and facilitate data transfer between the fluid and structure. This method allows the utilization of existing robust and accurate solvers, with the potential for additional coding required for the coupling component. As data transfer between the fluid and structure occurs only after discrete coupling intervals, this approach introduces errors when compared to the monolithic solution. The partitioned approach can further be categorized as explicit or implicit, depending on the frequency of solver iterations or the instances of interface data exchange during a single coupling timestep.

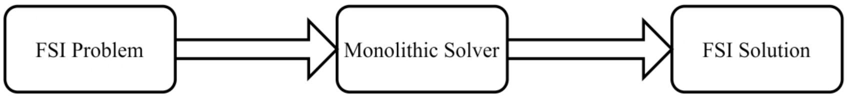

Figure 3.4: Schematic of Monolithic FSI Approach
[1]

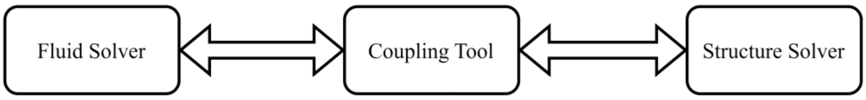

Figure 3.5: Schematic of Partitioned FSI Approach
[1]

3.6.2. Explicit Coupling

In the explicit coupling algorithm, the fluid and structure solvers are iteratively solved for a predetermined number of iterations, typically a single iteration. As a result, achieving proper kinematic and dynamic balance may be challenging. Consequently, explicit coupling can exhibit instability, particularly in scenarios involving strong interactions where significant structural displacements occur within a single timestep.

Explicit coupling can be further classified as either serial or parallel, depending on the order of execution. In serial explicit coupling, the first solver completes its timestep from t_n to t_{n+1} before the second solver executes its timestep, utilizing the solved boundary output from the first solver as its input. If x_1 and x_2 represent the input variables of solvers S_1 and S_2, respectively, the solution step in serial explicit coupling is expressed as follows:

$$x_2^{n+1} = S_1^n(x_1^n) \tag{3.45}$$

$$x_1^{n+1} = S_2^n(x_2^{n+1}) \tag{3.46}$$

In the parallel explicit coupling, both the solvers are executed simultaneously taking the input of the previous timestep in both the solvers.

$$x_2^{n+1} = S_1^n(x_1^n) \tag{3.47}$$

$$x_1^{n+1} = S_2^n(x_2^n) \tag{3.48}$$

3.6.3. Implicit Coupling

In the implicit coupling algorithm, the fluid and structure solvers undergo iterative resolution for numerous sub-iterations, involving the exchange of dynamic and kinematic interface data at each sub-iteration until convergence is achieved. Consequently, the implicit solution strives for the precision of a monolithic approach adhering to stringent convergence criteria, albeit at the cost of increased computational expense. Similar to explicit coupling, implicit coupling can be categorized as either serial or parallel.
The fixed point iteration equations for the serial implicit scheme are as follows;

$$x_2^{(n+1),i+1} = S_1^n(x_1^{(n+1),i}) \tag{3.49}$$

$$x_1^{(n+1),i+1} = S_2^n(x_2^{(n+1),i+1}) \tag{3.50}$$

Similarly, the equations for parallel implicit coupling scheme are written as;

$$x_2^{(n+1),i+1} = S_1^n(x_1^{(n+1),i}) \tag{3.51}$$

$$x_1^{(n+1),i+1} = S_2^n(x_2^{(n+1),i}) \tag{3.52}$$

Implicit coupling requires high computation costs as the number of sub-iterations increases with strict convergence criteria. For faster convergence, techniques like under relaxation and sophisticated quasi-Newton solvers are found to be used [22].

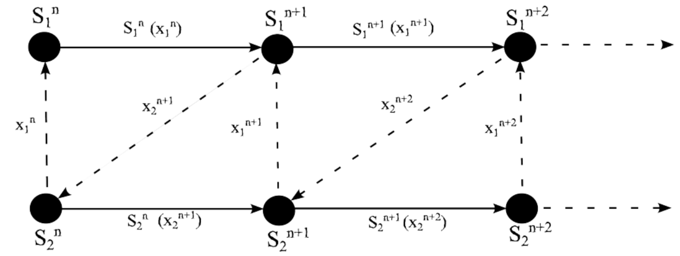

Figure 3.6: Schematic for serial coupling scheme [1]

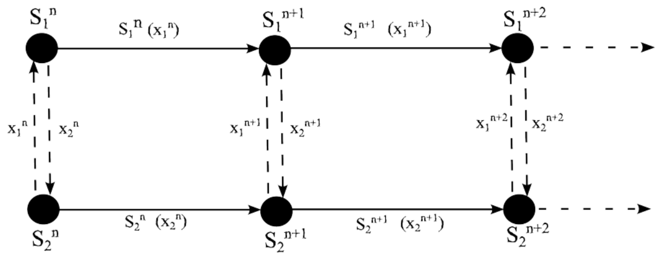

Figure 3.7: Schematic for parallel coupling scheme [1]

CHAPTER 4: METHODOLOGY

The flowchart below shows the methodology approach being followed for the project.

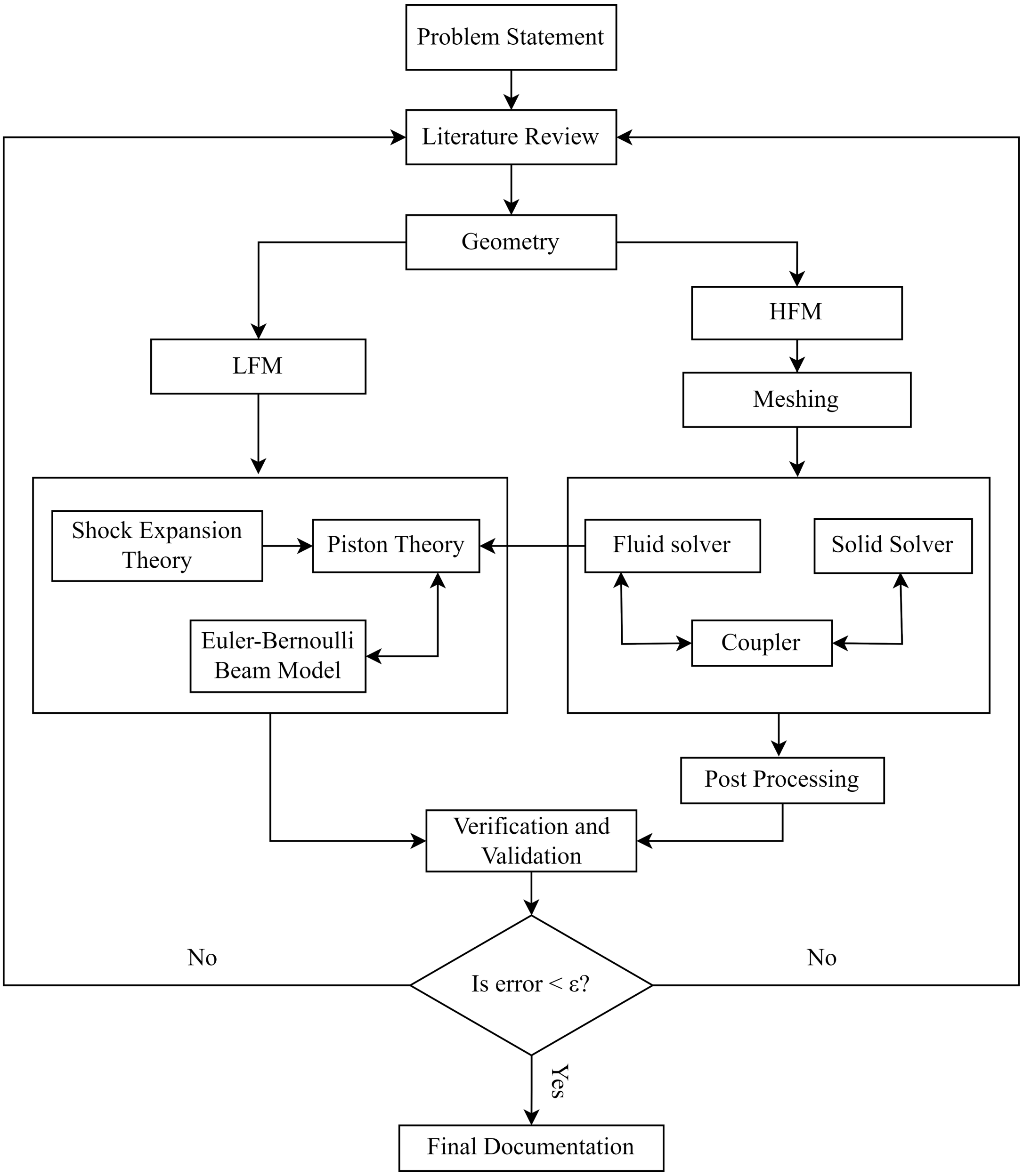

Figure 4.1: Methodology Flowchart

Two methods are applied for solving our problem: LFM and HFM. For the HFM, fluid solver OpenFOAM and solid solver CalculiX were coupled using coupling setup of preCICE. For the LFM, the pressure was calculated using either Shock-Expansion Theory, which uses analytical results for the pressure distribution or CFD results and Piston Theory for unsteady pressure approximations. The pressure is then fed to the 2D modelled plate using the Euler-Bernoulli beam model to solve the deflections.

4.1. Geometry

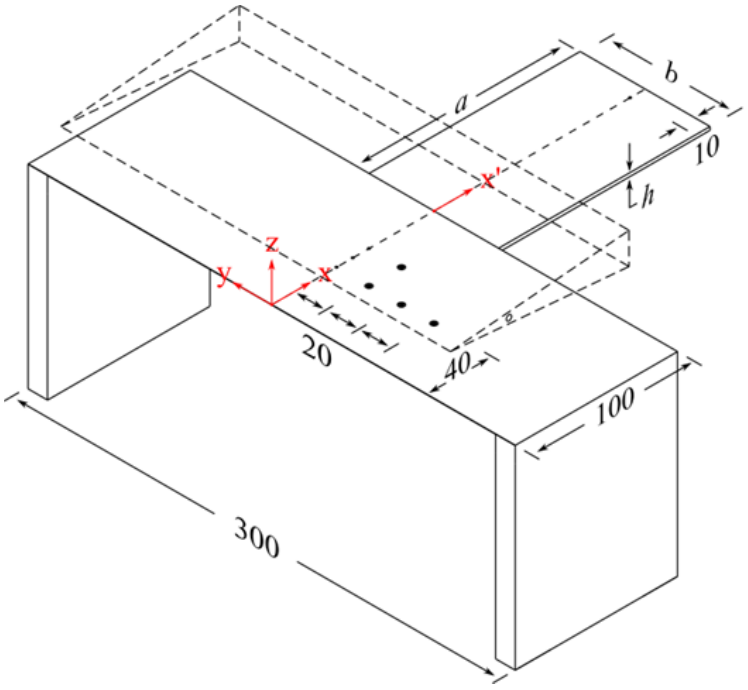

(a) 3D Geometry

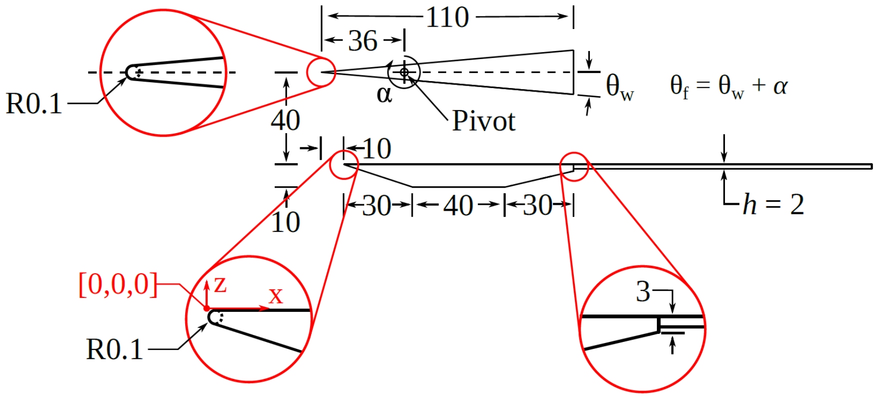

(b) 2D Geometry, image taken from [7]

Figure 4.2: Geometry from AePW3 / High Speed Working Group

The geometry used for the study is taken from the (AePW3/High Speed Working Group). The setup includes a wedge, a cantilevered compliant plate and a hammerhead as shown in figure 4.2. The wedge is symmetric with a half angle (θ_w) of 5°, which is 110 mm in length and has a span of 240 mm. It is pivoted about a pivot point 36 mm from the leading edge. It is free to pitch between -5° and 5° angle of attack, which results in a flow deflection angle range of 0° to 10°. The natural frequency of oscillation of the wedge is reported to be 42 Hz[6, 7]. The compliant plate is cantilevered with a 130 mm length, 80 mm span and 2 mm thickness. The plate is attached to the hammerhead with two rows of five countersunk screws equally spaced along the span to simulate a fully-bonded joint to simplify boundary conditions for simulation [7]. The hammerhead is 100 mm in length, 300 mm in span and 10 mm thick. It consists of a wedge forebody, a planar section and an expansion ramp. The expansion ramp of the hammerhead is truncated with a height of 3 mm to form a hinge line at the interface of the plate and hammerhead [7]. A 2D geometry for the setup is created for numerical simulation.

4.2. Operating Conditions

The freestream conditions for the study are taken from [7] and presented in table below. The test is done at Unit Reynold number (Re) of $7.1 \times 10^6 m^{-1}$ for 200 ms [23].

Table 4.1: Operating Conditions

M_∞	P_∞	T_0	T_∞	U_∞	γ	μ_∞
5.8	$590 Pa$	$575 K$	$75 K$	$985 m.s^{-1}$	1.4	$4.66e-06\ Pa-s$

4.3. Low Fidelity Modeling

In Low Fidelity Modelling, we modified the solver developed by [1] to account for the transient pressure on top of the plate. The solver developed by [1] was already verified for the HyFoil experiment [4]. The plate is represented as a cantilever beam using the Euler-Bernoulli beam model. The pressure on the upper surface of the plate is determined using the Shock-Expansion theory as given in section 3.3, assuming a flat plate geometry. The pressure on the lower surface of the plate is assumed to be 590 Pa, equal to the free-stream pressure. The deflection of the plate is calculated by solving the differential equation using the ode45 function in MATLAB. Also, the pressure on the top surface of the deflected plate is obtained by applying the piston theory.

4.3.1. Shock Expansion Theory

The time-varying pressure on the top surface of the plate, due to the oscillating shock generator, was obtained from the shock expansion theory. The pressure acting on top

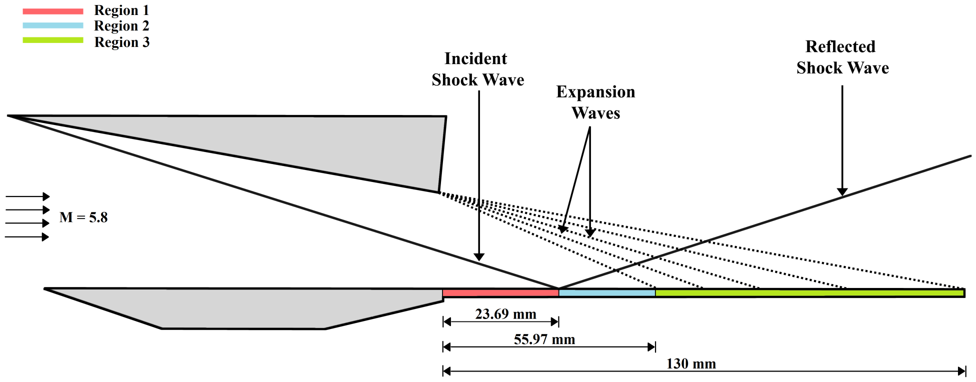

Figure 4.3: Schematic for analytical inviscid flow

of the plate surface was calculated when the plate was undeformed using the θ-β-Mach relation given in equation 3.1 as shown in figure 4.3. The geometry of expansion fan was calculated using Prandtl-Meyer equation given by equation (3.6). The plate was divided into three region by shock wave and expansion fan as shown in figure (4.5). The pressure in region was equal to free stream pressure (590 Pa). Region 2 was characterized by pressure after reflected shock. Region 3 consisted expansion fan and shock wave interaction. The pressure was estimated by dividing the flat plate into 26 equal segments.

4.3.1.1 Comparison of pressure distribution

The time-varying pressure distribution along the plate's length was determined by using shock-expansion theory. The plate was discretized into 26 elements, each with a length of 5 mm, to calculate the pressure distribution along the plate surface in regions 1, 2, and 3, as depicted in figure 4.3. This distribution was compared to the pressure distribution obtained from inviscid Fluid-Structure Interaction (FSI) simulation at time t = 0 when flow deflection angle was 10 degrees as shown in figure 4.4. The pressure distribution observed on the plate's surface exhibited discrepancies. These inconsistencies could arise from differences in the nature of the pressure distributions obtained: the inviscid Fluid-Structure Interaction (FSI) provides results for a transient case, whereas the pressure distribution derived from shock expansion theory pertains to a steady case. Additionally, numerical diffusion of pressure resulting from the numerical schemes employed could also contribute to these discrepancies.

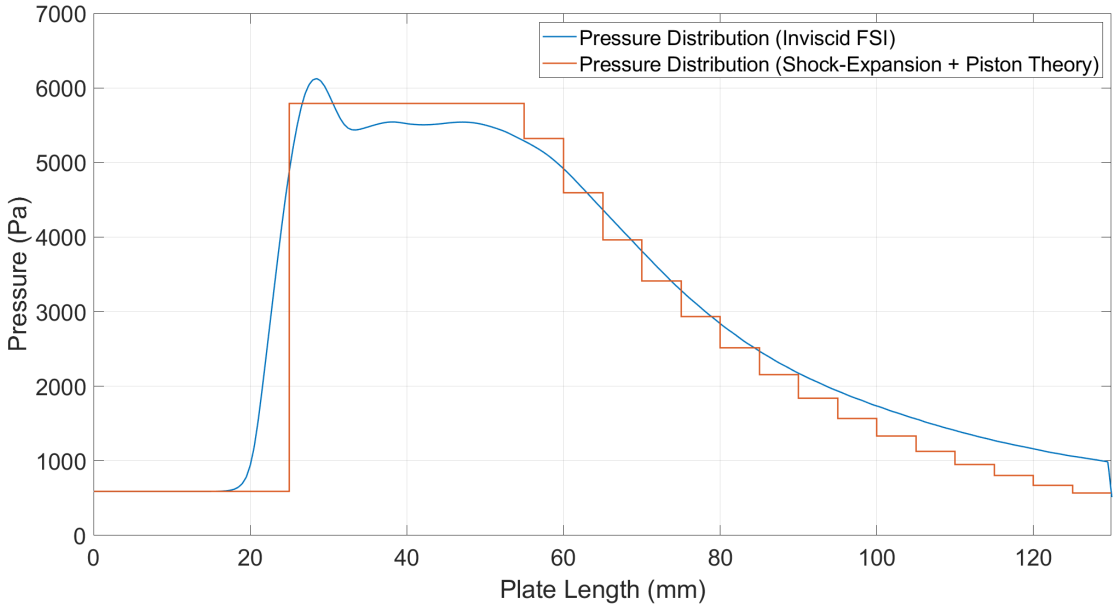

Figure 4.4: Comparison of pressure distribution along plate length obtained from shock-expansion theory and inviscid FSI at time t = 0 ms where $\theta_{flow} = 10^{\circ}$

4.3.2. Finite Element Method

The second-order ordinary differential equation given in (3.32) was solved by converting it into first-order by representing it in state space form. Then using ode45 function in MATLAB, the equation was solved to obtain displacement of finite element nodes.

4.3.3. Piston Theory

The pressure distribution on the upper surface of a flat plate after deflection was determined using second-order piston theory. This theory was applied at every instance except the first step, where the plate is undeformed. In piston theory, the input parameters were the local pressure, local Mach number over the flat plate element, and the inclination angle of the element. The output parameter was the pressure on the plate element after it underwent deflection. This pressure was then used to calculate the displacement in the next iteration.

4.3.4. CFD Enriched Piston Theory

To improve the accuracy of LFM, an inviscid fluid simulation was performed in OpenFOAM using 31.4K cells with an oscillating shock generator. The pressure and mach number values were extracted from the upper surface of the plate. The pressure distribution was averaged for 26 elements as shown in figure 4.5. These values, along with displacement values obtained by solving the ODE given in equation 3.32, were input into piston theory to calculate the pressure on the deflected plate. This pressure was then used to calculate the displacement in the next iteration.

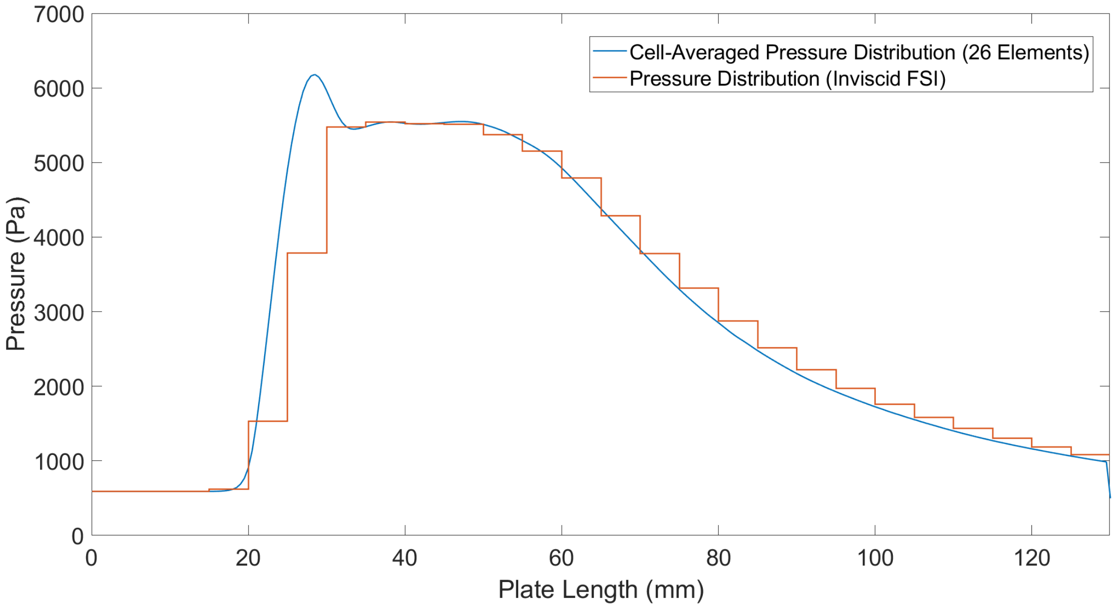

Figure 4.5: Cell averaged pressure distribution obtained from numerical simulation (t = 0 ms where θ_{flow} = 10°)

4.4. High Fidelity Modeling

In High Fidelity Modelling, the fluid flow field is solved by rhoCentralFoam, a density-based solver in Open-source Field Operation and Manipulation (OpenFOAM), CalculiX is used to solve the structural deformation, and the solvers are coupled using a coupling library,preCICE. The partitioned approach is followed for FSI simulation. This is because the partitioned approach has the advantage of modularity and thus can incorporate state-of-the-art improvements [24].

4.4.1. Case Setup

4.4.2. Fluid Case Setup

The domains used in the inviscid and viscous simulations are shown in the figure 4.6 and figure 4.7. The viscous domain contains the hammerhead with a blunt edge of radius 0.1 mm to better emulate experimental conditions.

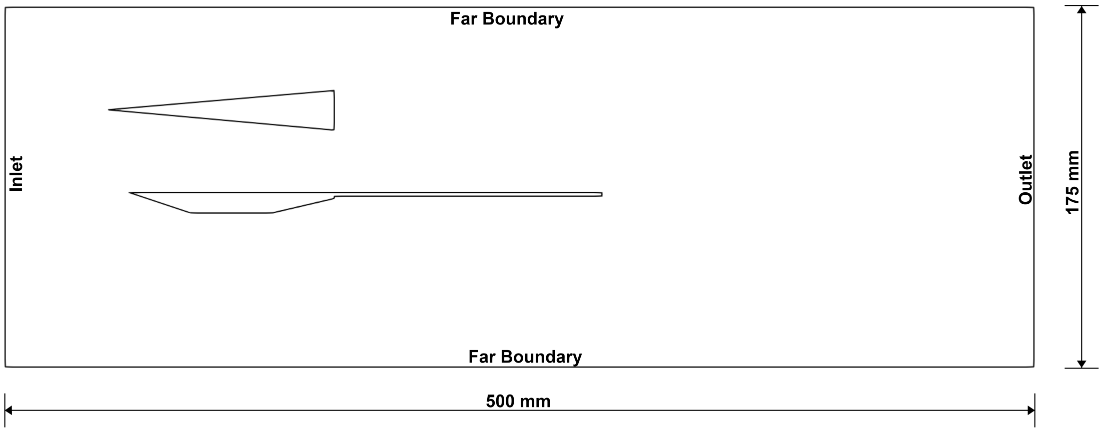

Figure 4.6: Domain for Inviscid flow

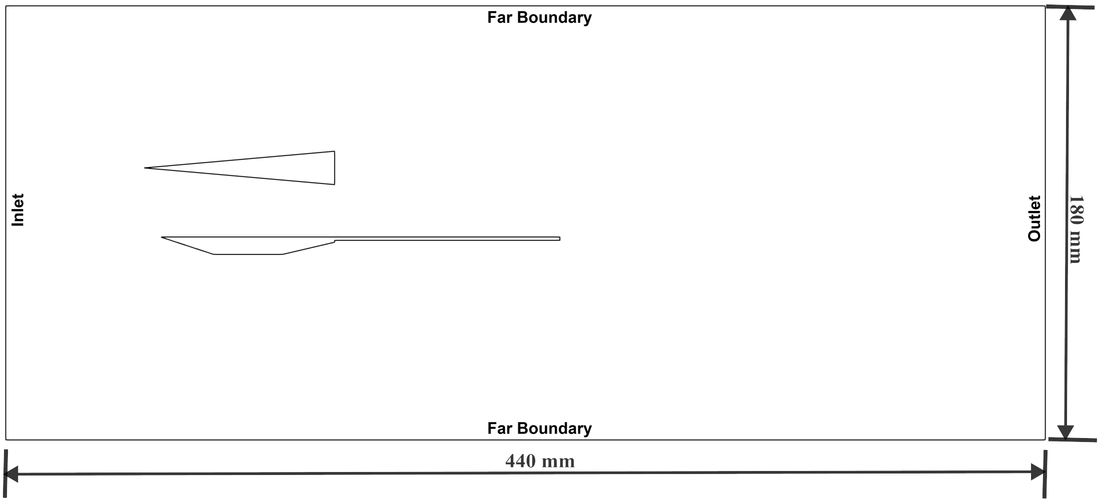

Figure 4.7: Domain for Viscous flow

4.4.2.1 Geometric Discretization

Structured mesh was created for the domain using blockMesh utility in OpenFOAM. Different grids will be used for running the viscous and inviscid simulations. The final mesh for the simulation was created after performing a grid convergence study for both the cases.The grids in the inviscid case have been refined in the region between the plate and the wedge to capture the various shockwave interactions and shock-expansion wave interactions.

In the viscous case, the blunt edge around the hammerhead has been refined to capture the bow shock that forms ahead of it. Grading has been done in the vertical direction above the plate to capture the boundary layer. Similar to the inviscid case, the region between the plate and the wedge, has been refined to capture the various interactions between the shock waves and the expansion waves, the phenonmenon of SWBLI and bow shock transition. The grids in the other regions are the result of compromise between the mesh growth and the computational cost.

Inviscid Grid Convergence Study

Grid refinement technique was used for the grid convergence study. Firstly, a coarse mesh was created for which the solution could be obtained. Then the mesh count was increased by a factor of 2 and 3 to obtain the medium and fine mesh respectively. Thus, a set of three mesh was used for the study. For the inviscid mesh, peak pressure was chosen as the convergence test parameter. Then a general procedure of Richardson extrapolation was followed for variable r to calculate the peak pressure value when $\Delta x \rightarrow 0$ and$\Delta y \rightarrow 0$ [25]. Here, r = h_1/h_2, where h_1=discrete spacing of fine grid and h_2=discrete spacing of coarse grid. Order of convergence (p) equal to 1.87 and the peak pressure equal to 6167.55 Pa was obtained.

Table 4.2: Inviscid Grid Convergence Study

Grid	Number of cells	Peak Pressure (Pa)	Percentage error from extrapolated value
Coarse	16706	6102.9	1.0478%
Medium	31479	6147.7	0.3214%
Fine	49227	6158.9	0.1398%

Calculations were then performed to obtain the grid convergence index (GCI) using a factor of safety of 1.25.

Table 4.3: G.C.I for Inviscid Mesh

Grid-transition	G.C.I
Coarse-Medium	0.403
Medium-Fine	0.1749

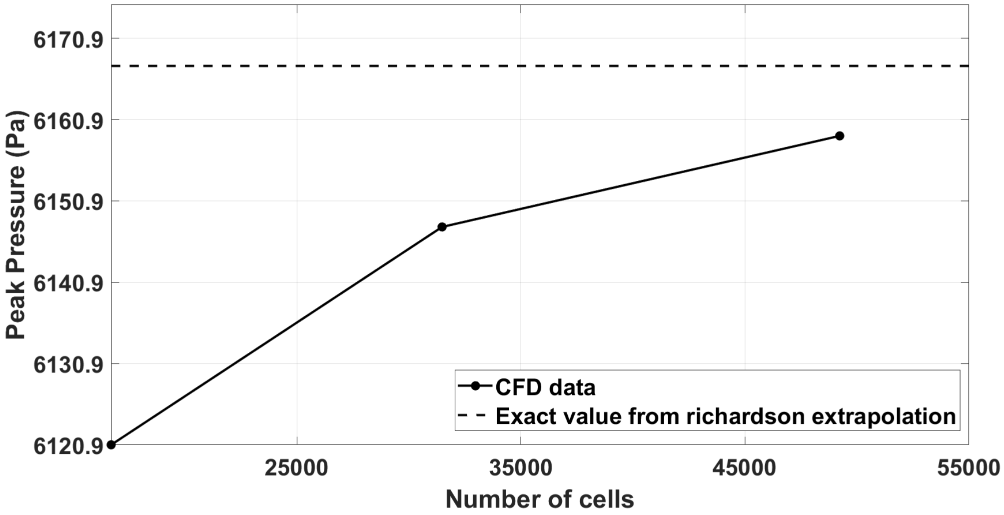

Figure 4.8: Grid convergence for inviscid simulation

Convergence criteria were set G.C.I < 0.2. Since the medium-fine transition was within the convergence criteria and the medium mesh was within the asymptotic range of convergence with an error of 0.32%, the medium mesh with 31479 cells was declared converged. The converged mesh's parameters are tabulated in table 4.4 and figure 4.9 illustrates converged mesh for the inviscid case.

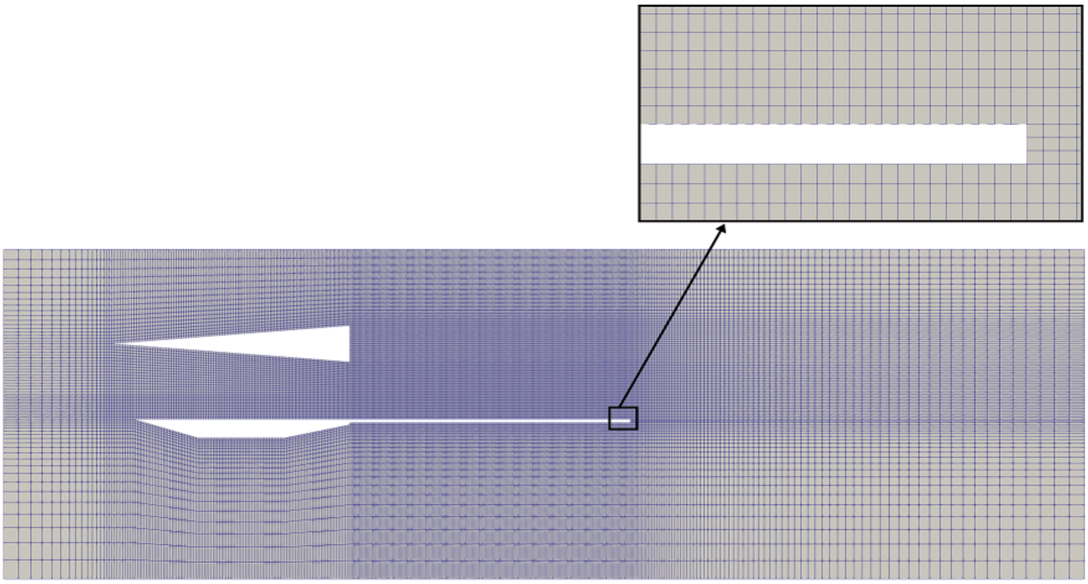

Figure 4.9: Converged mesh for inviscid simulation

Table 4.4: Parameters of Converged Mesh

Number of cells	min Δx (mm)	max Δx (mm)	min Δy (mm)	max Δy (mm)
31479	0.706	7	0.67	10

Viscous Grid Convergence Study

Similar to the inviscid grid convergence study, we used a grid refinement technique, increasing the mesh count by factors of 2 and 4 from the initial coarse mesh to generate medium and fine meshes, respectively. For the viscous mesh, boundary layer reattachment point was chosen as the convergence test parameter. Then utilizing the identical methodology as used in the inviscid case, the order of convergence p equal to 3.1, extrapolated value of reattachment point from leading edge equal to 140.0437 mm and G.C.I was obtained.

Table 4.5: Viscous Grid Convergence Study

Mesh	Number of cells	Boundary layer reattachment point	Percentage error
Coarse	35594	136.93 mm	2.22%
Medium	71281	139.72 mm	0.23%
Fine	142806	140.001 mm	0.0304%

Table 4.6: G.C.I for Viscous Mesh

Mesh-transition	G.C.I
Coarse-Medium	0.29
Medium-Fine	0.030084

Similar to the inviscid case, convergence criteria was set G.C.I < 0.2. Since the medium-fine transition was within the convergence criteria, and the medium mesh was within the asymptotic range of convergence with an error of 0.23%; the medium mesh with 71281 cells was declared converged. The parameters of the converged mesh are tabulated in table 4.7. Here, y_f represents height of first layer while y_l represents height of last layer in the boundary layer.

Table 4.7: Parameters of Converged Mesh

Number of cells	BL Δx (m)	y_f (m)	y_l(m)	max Δy (m)	max Δx (m)
71281	7e$-$4	14.44 e$-$6	3.61 e$-$4	0.010376	0.00704056

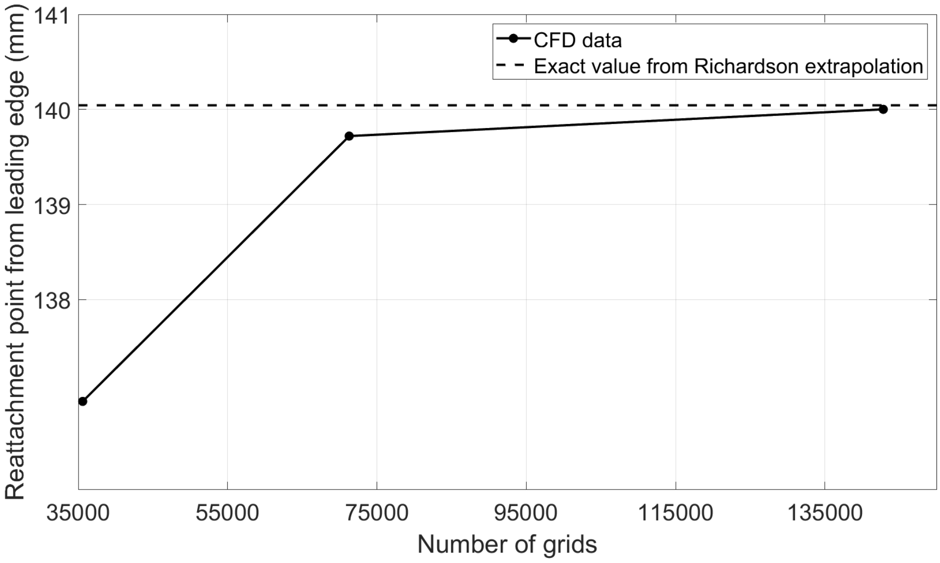

Figure 4.10: Grid convergence for viscous simulation

The final simulation is carried out in a mesh slightly more refined than the converged mesh as shown in figure 4.11 and its parameters are tabulated in table 4.8. The boundary layer grid for both the converged and the final mesh was 1.9168 mm from the plate.

Table 4.8: Parameters of Final Mesh for viscous simulations

Number of cells	BL Δx (m)	y_f (m)	y_l(m)	max Δy (m)	max Δx (m)
105546	4.925e−4	11.67e−6	3.90869e−4	0.00366876	0.0033113

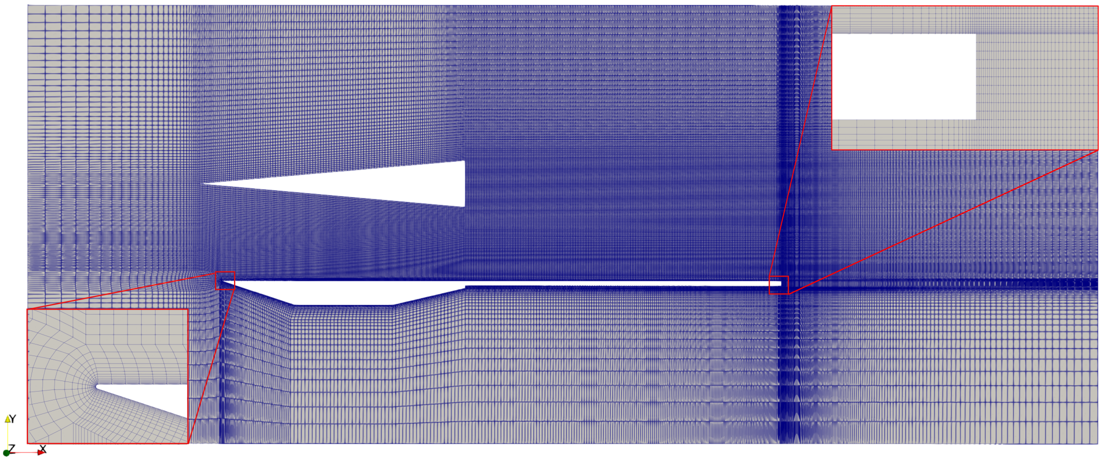

Figure 4.11: Final mesh for viscous simulation

4.4.2.2 Initial and Boundary Conditions

The initial and boundary conditions used in the simulation are tabulated in table 4.9, table 4.10 and table 4.11.

Table 4.9: Initial Flow Conditions

Flow variable	P_∞	T_w	T_∞	U_∞
Value	$590Pa$	$300K$	$75K$	$985m.s^{-1}$

Table 4.10: Boundary Conditions for Inviscid Simulations

Domain	Pressure	Velocity	Temperature	Point Displacement
Inlet	zeroGradient	fixedValue	fixedValue	zeroGradient
Plate	zeroGradient	Slip	fixedValue	fixedValue
Farboundary	zeroGradient	supersonic Freestream	inletOutlet	fixedValue
Wedge	zeroGradient	Slip	fixedValue	solidBodyMotion Displacement
Hammerhead	zeroGradient	Slip	fixedValue	fixedValue
Outlet	wave Transmissive	supersonic Freestream	inletOutlet	zeroGradient

Table 4.11: Boundary Conditions for Viscous Simulations

Domain	Pressure	Velocity	Temperature	Point Displacement
Inlet	zeroGradient	fixedValue	fixedValue	zeroGradient
Plate	zeroGradient	noSlip	fixedValue	fixedValue
Farboundary	wave Transmissive	supersonic Freestream	inletOutlet	fixedValue
Wedge	zeroGradient	noSlip	fixedValue	solidBodyMotion Displacement
Hammerhead	zeroGradient	noSlip	fixedValue	fixedValue
Outlet	wave Transmissive	supersonic Freestream	inletOutlet	zeroGradient

An oscillating motion was induced in the wedge by assigning the solidBodyMotionDisplacement condition in point displacement file. The induced motion was given about the pivot point of the wedge and its frequency and amplitude were tuned according to the data provided by experiment, where the frequency was reported to be 42 Hz. However, the oscillation profile of the wedge tracked in the experiment shows that the oscillation was damped which is evident in the comparison shown in figure 4.12. The damped nature of oscillation in the experiments can be contributed to friction whereas aerodynamic damping can be assumed negligible [14, 26].

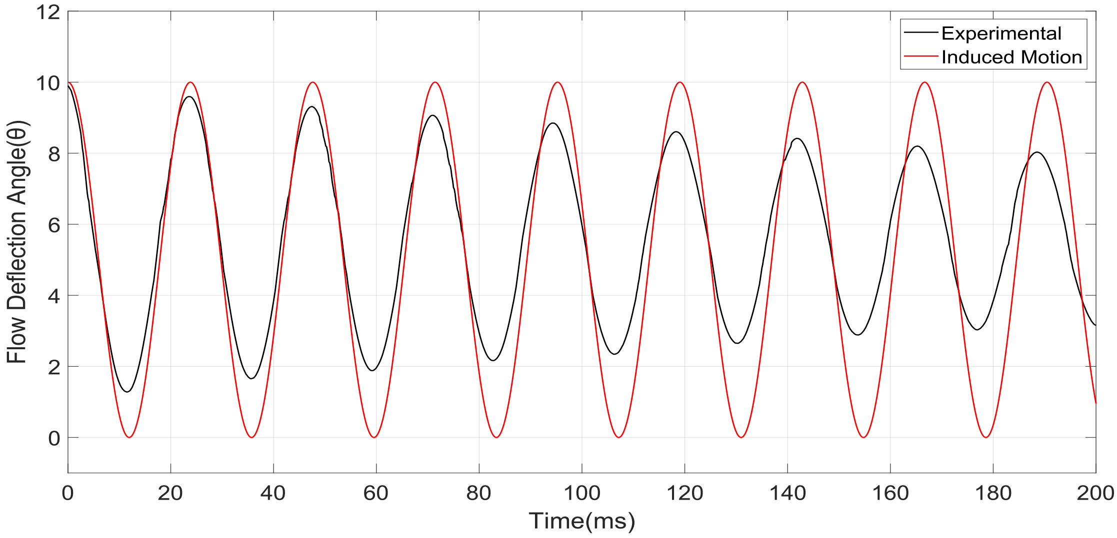

Figure 4.12: Comparison of the oscillation profile of the wedge in the experiment and simulation

4.4.2.3 Discretization Schemes

The discretization schemes used in the inviscid and viscous case are tabulated in table 4.12 and 4.13.

Table 4.12: Discretization Schemes for Inviscid Simulations

Parameters	Discretization Scheme	Order of accuracy
Flux	Kurganov	Second Order
Time Derivative	Euler	First order
Gradient	Gauss Linear	First order
Divergence	Gauss vanLeer	Second Order
Laplacian	Gauss linear corrected	First Order
Interpolation	Minmod	Second Order

Table 4.13: Discretization Schemes for Viscous Simulations

Parameters	Discretization Scheme	Order of accuracy
Flux	Kurganov	Second Order
Time Derivative	Euler	First order
Gradient	Gauss Linear	First order
Divergence	Gauss Linear	First Order
Laplacian	Gauss Linear Limited	First Order
Interpolation	Minmod	Second Order

4.4.2.4 Solution Methods and Tolerances

For inviscid simulations, variables of governing equations (rho, rhoU, rhoE) were computed explicitly using a diagonal solver. The velocity vector and energy were computed using smoothSolver and Gauss-Seidel was selected as the smoother to converge the solution to required tolerance. The cell displacement was computed using GAMG solver. Tolerance and relative tolerance for velocity vector and energy was set to $1e-9$ and 0 while tolerance and relative tolerance for cell displacement were set to $1e-8$ and 0 respectively. For the viscous simulations, the variables of governing equations (rho,rhoU,rhoE) were also computed explicitly using a diagonal solver. Velocity vector and energy were computed using smoothSolver and Gauss Seidel was selected as the smoother to converge the solution to required tolerance, while cell displacement was computed using smoothsolver using Symmetric Gauss Siedel as smoother. Tolerance and relative tolerance for velocity vector was set to $1e-11$ and 0, for energy was set as $1e-10$ and 0 while for cell displacement tolerance and relative tolerance was set as $1e-8$ and $1e-4$.

4.4.2.5 Dynamic Mesh

Dynamic mesh was configured in the dynamicMeshDict file, where mesh diffusivity and motion solver to be used were defined. The type of motion was set in dynamicFvMesh entry, where dynamicMotionSolverFvMesh was entered to simulate motions in the domain. DisplacementSBRstress was defined as the motion solver for the wedge and this was read for the whole domain as well. The diffusivity coefficient for both the plate and the wedge were defined as quadratic inverse from the plate/wedge, which implies that diffusivity decreases quadratically away from the object.

4.4.3. Solid Case Setup

4.4.3.1 Geometric Discretization

The mesh for the solid was generated using PrePoMax. A structured quadrilateral mesh having grid resolution of 0.5mm in all directions was created and used for both inviscid and viscous simulations.

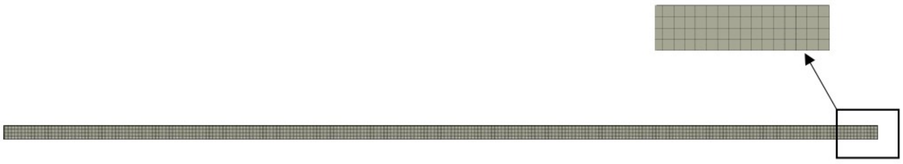

Figure 4.13: Solid Mesh

4.4.3.2 Material Properties and Boundary Conditions

All the material properties as required by the .inp file for CalculiX solver are taken from [7]. The material properties given to the solver are tabulated in table 4.14. A fixed support was applied at the end of the plate to emulate a cantilevered plate. This was done by grouping the nodes of the end of the plate and restricting their motion in all directions. The nodes everywhere else were fixed in the z-direction and were free to move about x and y directions. Nodes at contact surface of the plate were grouped as interface.

Table 4.14: Material Properties of Plate

Properties	Value
Density	2690 kg/m^3
Flexural Modulus	52.7 Gpa
Poisson's ratio	0.33

4.4.3.3 Modal Analysis

Two-dimensional modal analysis of a cantilever plate was conducted using a plate with dimensions of 130x80x2 mm with a material having properties given in table 4.14. The nodes at the extreme side of one of the faces, measuring 80mm x 2mm were fixed. This was done to loosen the boundary condition on the cantilever plate to better emulate the experiment.The results obtained are shown in table 4.15.

Table 4.15: Modal Analysis

Mode	Frequency
Mode 1	87.855 Hz
Mode 2	544.97 Hz
Mode 3	1484.75 Hz

The Rayleigh Damping coefficients were calculated using equation 3.37 and 3.38 with $\zeta = 0.0045$ [7]. We obtained $\alpha = 4.2783$ and $\beta = 2.2635 * 10^{-6}$.

Modal analysis of the cantilever plate was also carried out using LFM in two dimensions by calculating the eigenvalues of the mass and stiffness matrices, as described in equations 3.40 and 3.41. The resulting mode shapes with their corresponding frequencies are illustrated in figure 4.14. A comparison was made between the frequencies obtained from LFM and those from Finite Element (FE) simulation, as presented in table 4.16. The results showed a close agreement, with an error of 2.4% for the first mode and 3.48% for the second mode. The damping matrix calculations only required the frequencies of the first and second modes.

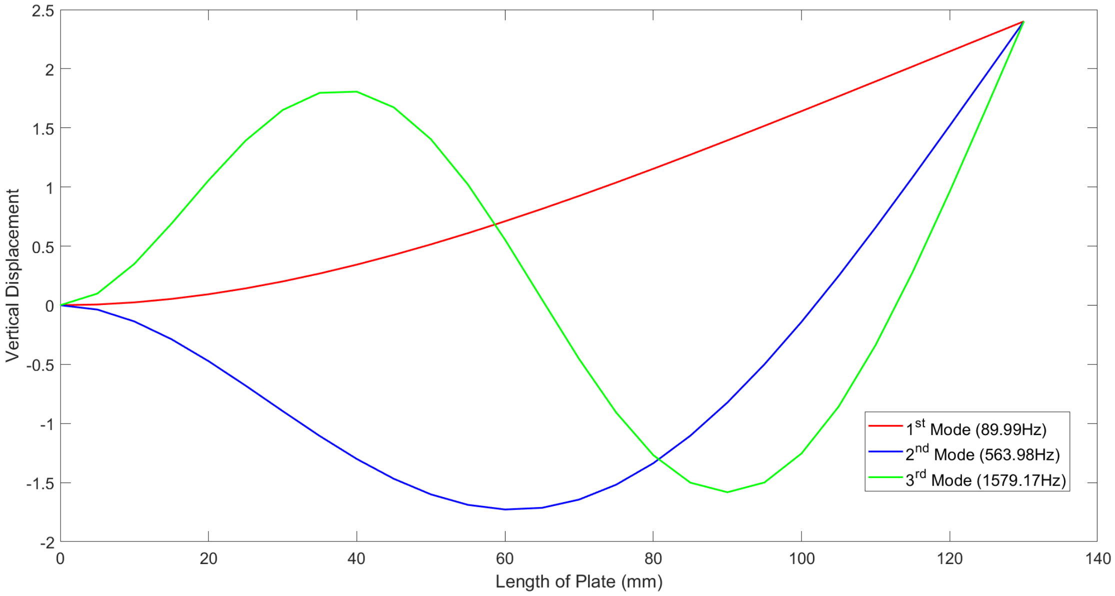

Figure 4.14: Mode shape of oscillation of cantilever plate obtained from LFM

Table 4.16: Comparison of frequency of modes obtained from LFM and FE simulation

Mode	Frequency (LFM)	Frequency (FE simulation)
1	89.99 Hz	87.855 Hz
2	563.98 Hz	544.97 Hz
3	1579.17 Hz	1484.75 Hz

4.4.3.4 Discretization and Solution Method

The time domain is discretized using the direct implicit time integration method while spatial discretization was done using FEM. Symmetric Spooles solver was used for the dynamic analysis of the plate.

4.4.4. FSI Coupling Setup

The setup of coupling between the fluid and the solid solver was done using the preCICE adapter. The coupling setup was configured in the precice-config.xml file. Serial explicit coupling scheme was used with a coupling time of 0.1 ms for inviscid simulations. Fluid was set as the first participant and solid was set as the second participant, which means that the fluid solver runs until the coupling time then maps the force data to nodes of the solid using nearest neighbour mapping. The solid then proceeds to calculate the displacement of the nodes and maps it back to fluid node using the same algorithm. For the viscous simulations, the coupling time was set to $1e-6$. Similar to inviscid simulations, serial explicit coupling scheme was used with fluid as first and solid as second participant.

Explicit coupling was chosen over implicit coupling because the analysis done previously indicated that implicit coupling, despite taking nearly three times longer to solve, showed minimal differences in results [1].

CHAPTER 5: RESULTS AND DISCUSSIONS

5.1. Shockwave Boundary layer interaction

As discussed earlier rotatory oscillating motion of wedge creates periodically oscillating shock impingement location on plate. As the wedge oscillates with frequency of 42 Hz, shock impingement location also changes in similar manner.

To observe the shockwave boundary layer interaction, the relevant flow features can be observed from the solution at a particular instant. For this, a numerical schlieren ($\frac{\delta \rho}{\delta y}$) at an instant T = 23.2 ms was taken, where the flow deflection angle was maximum i.e. 10 degrees. The flow features captured are shown in figure 5.1. As hypersonic uniform flow comes across the shock generator, a strong incident oblique shock wave is generated. The shock impingement creates strong adverse pressure gradient on the cantilever plate, leading the boundary layer to separate, recirculation of flow and the formation of a separation bubble. Now, the flow sees separation bubble as an obstacle and creates a separation shock. Impingement location shifts upstream. Flow at top of the separation shock expands to form expansion fan and shortly downstream the flow reattaches and forms reattachment shock. The interaction between shock wave and expansion fan has curved the shock wave away from the plate. Another observation can be made behind the wedge where two expansion fans interact to form weak oblique shocks. Pressure contour of the flow field at the same time instant is shown in figure 5.2.

The pressure profile obtained on the hammer head and the plate matches the expected pressure distribution as shown in figure 5.3, with the pressure rising on the region after the separation shock. A pressure plateau is observed on the recirculation region, which is inside the separation bubble. After the reattachment point, there is increase in pressure as the flow passes through reattachment shock and another plateau is observed. The pressure decrease observed afterwards is due to interaction between the flow and the expansion fan from the wedge.

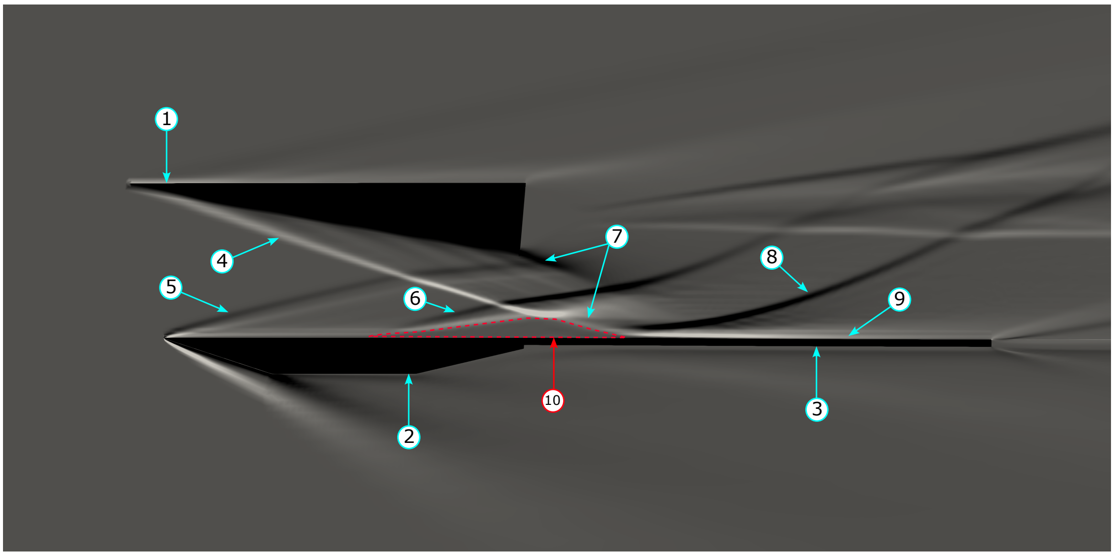

Figure 5.1: Instantaneous numerical schlieren as shock generator reaches maximum flow deflection angle (10°). Flow features: 1. Shock generator 2. Hammerhead 3. Cantilever plate 4. Incident shock 5. Hammerhead leading edge shock 6. Separation shock 7. Expansion fan 8. Reattachment shock 9. Boundary layer 10. Laminar separation bubble

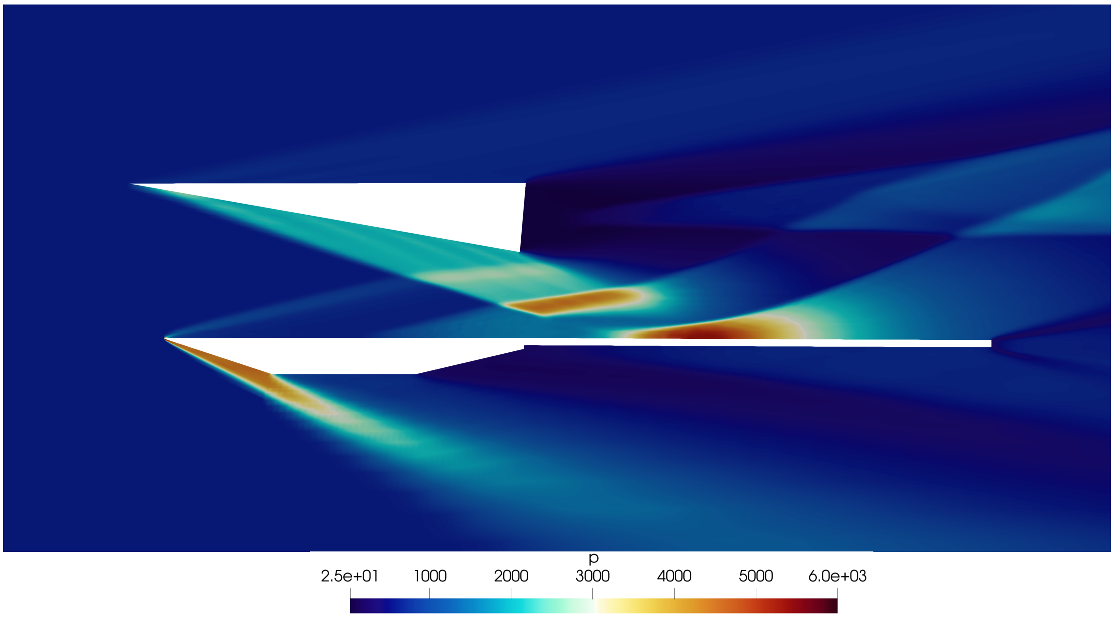

Figure 5.2: Pressure contour of the flow field

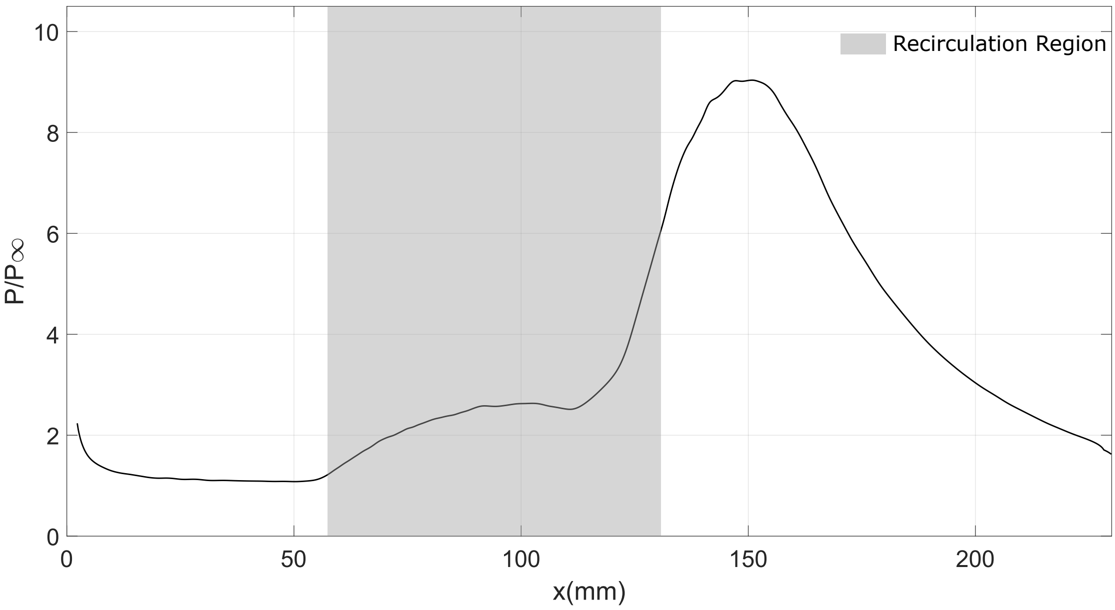

Figure 5.3: Pressure distribution over the hammerhead and plate at T=23.2 ms

5.2. Separation Bubble Dynamics

In this section four instances of the schlieren images are compared with the numerical schlieren at the same instant of the test duration. Numerical schlieren corresponds to the density gradient of the flow field. In this particular study, density gradient is taken along vertical direction i.e, $\frac{\delta\rho}{\delta y}$. to better match the schlieren images from the experiment. The first time instant t'= 0 is taken at 17.2 ms after the start of the test. Figure 5.5 compares four instances t'= 0, 2, 4 and 6 ms of schlieren images with numerical schlieren at the same instances. Shock impingement location shifts upstream as flow deflection angle increases with increasing time instances. At each instant the size of separation bubble grows in size as the flow deflection angle and adverse pressure gradient increases.

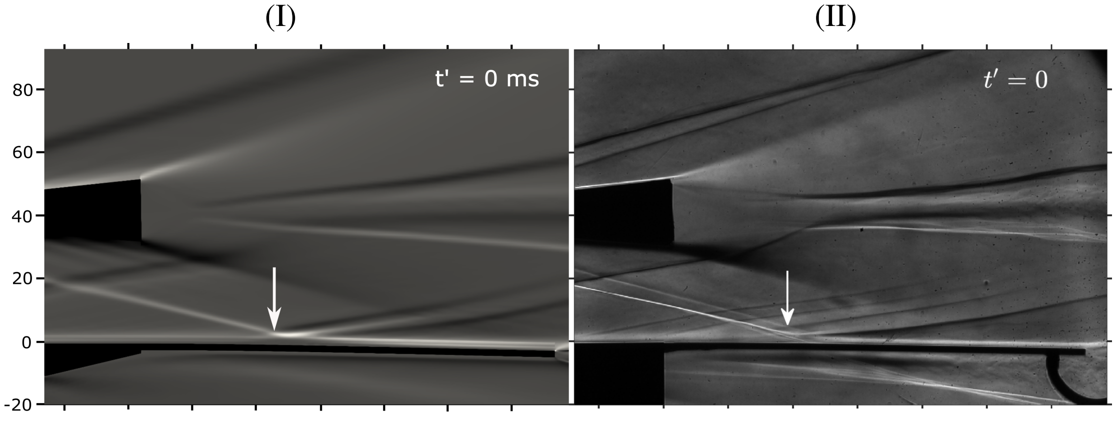

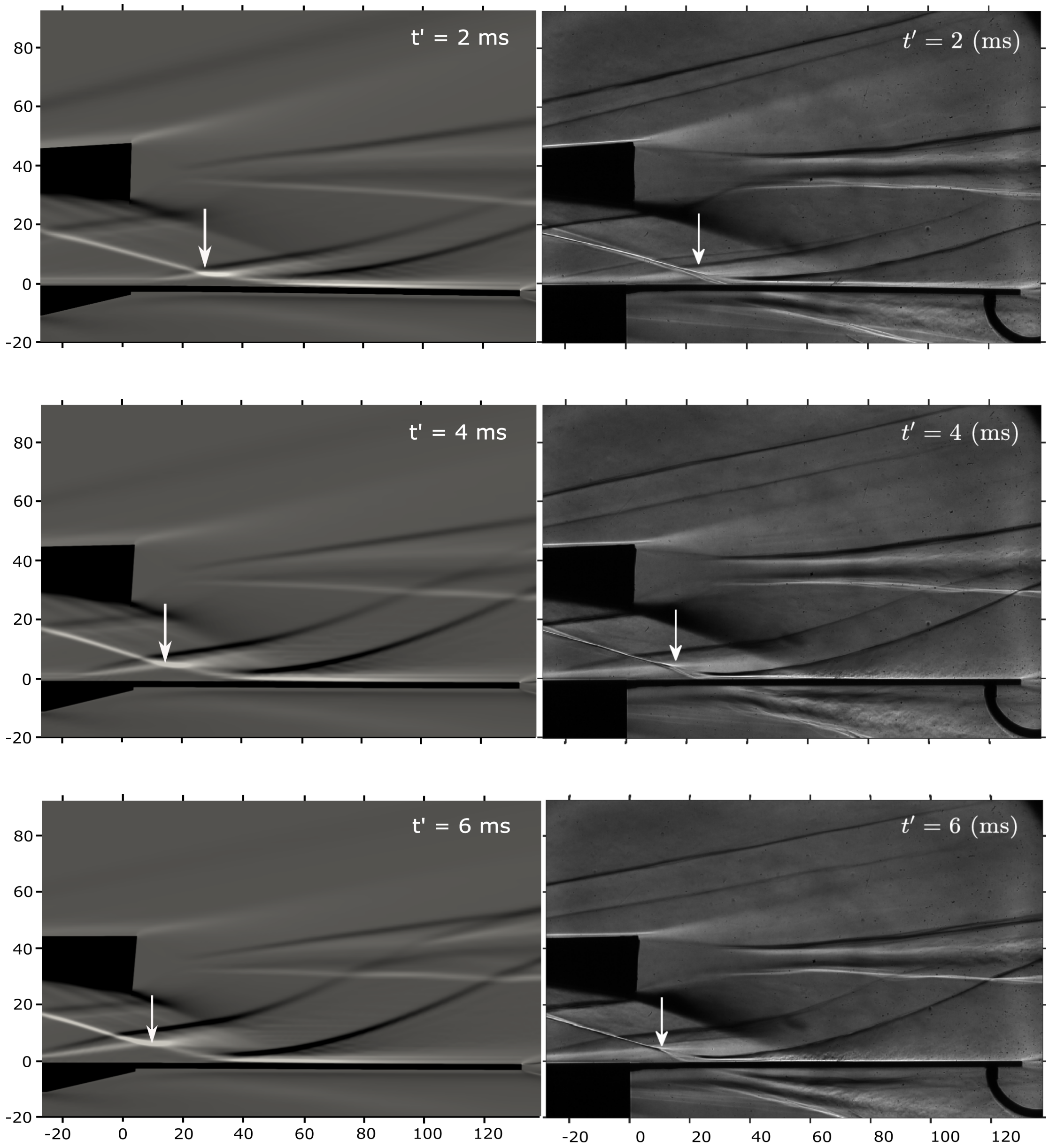

Figure 5.5: Instantaneous schlieren images obtained from computations($\frac{\delta\rho}{\delta y}$) (I), normalized density gradient along vertical direction and experiment(II). Arrow indicates the shock impingement location

The nature of separation bubble and flow separation can be more explored with wall shear stress evolution along the surface of hammerhead and cantilever plate. Dip in wall shear stress at recirculation region clearly indicates the separation is laminar in nature. Wall shear stress evolution at each time instant is shown in figure 5.6. We can clearly see the flow separation point, which is denoted by transition of wall shear stress from positive to negative, shifts upstream. Separation bubble becomes progressively larger in increasing time instances due to the stronger oblique shock wave as flow deflection angle increases. The size of separation bubble at each instant is shown in table below.

Table 5.1: Size of separation bubble

Time Instant	Length
t’ = 0 ms	29.207 mm
t’ = 2 ms	39.279 mm
t’ = 4 ms	57.014 mm
t’ = 6 ms	71.036 mm

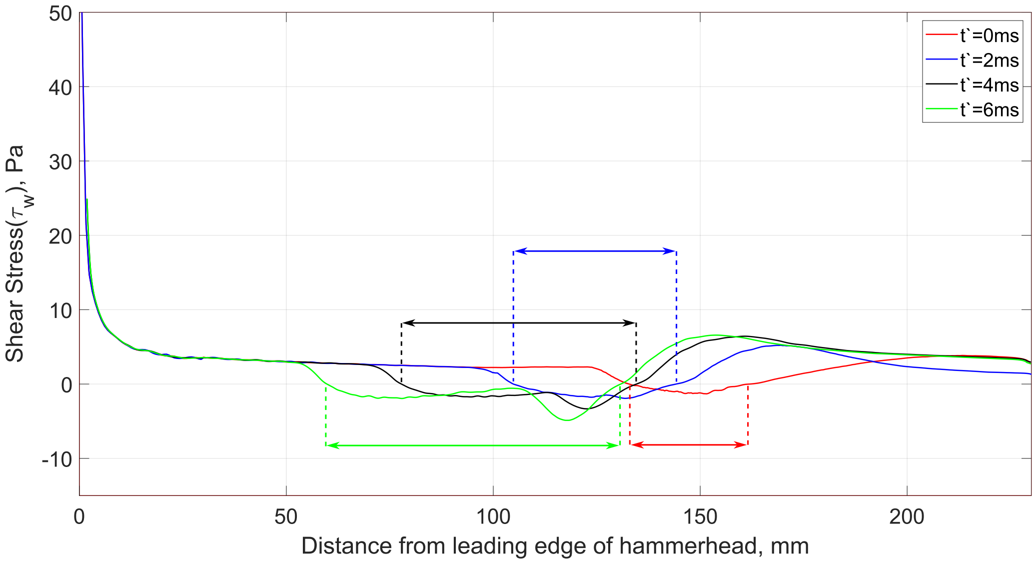

Figure 5.6: Wall shear stress at each time instant. Red, blue, black and green arrow represent the length of the separation bubble at time instant t’ = 0 ms, 2 ms, 4 ms and 6 ms respectively.

5.3. Pressure Based Analysis

5.3.1. Pressure Distribution over Cantilever Plate

Local coordinate system is established in the pressure trend plot where x' = 0 mm corresponds to the fixed end of the cantilever plate. In figure 5.7, pressure evolution normalized with free stream pressure (P_∞ = 590 Pa) over the surface of cantilever plate of viscous and inviscid simulation is compared with the pressure evolution obtained from the experimental data. We can clearly see the shock impingement location has shifted upstream as time progresses. Impingement location is further downstream compared to viscous and experimental result in inviscid case as there is no SWBLI and thus no separation bubble. Also the pressure plateau before shock impingement is slightly larger in experiment because of flow separation shock which is again absent in inviscid simulation. Beside these downsides of inviscid case, the pressure evolution is consistent with the experimental result.

In viscous simulation, the shock impingement location is still downstream compared to experimental result at t' = 0ms as shown in figure 5.5 and 5.7, however it matches very good in rest of the time instances. The rise in pressure after reattachment shock is slightly less steep compared to experimental result. However, the decrease in pressure after interaction with expansion fan is consistent with experimental result in both inviscid and viscous simulations. Also the peak pressure at each time instances is under predicted by inviscid as well as viscous simulation.

Beside these slight deviations, viscous pressure trend matches very consistently with experimental results. Pressure evolution is obtained with image processing of pressure sensitive paint over the surface of cantilever plate and then normalized with average freestream pressure of 590 Pa in the experiment. Red dashed lines in experimental data is the location of static pressure tap [4]. In each instant the peak pressure value in Viscous CFD better matches the experimental data in comparision to Inviscid FSI The peak pressure value increased by around 4.1% (227.3 Pa) in viscous result when compared to inviscid result at maximum flow deflection angle i.e t' = 6ms.

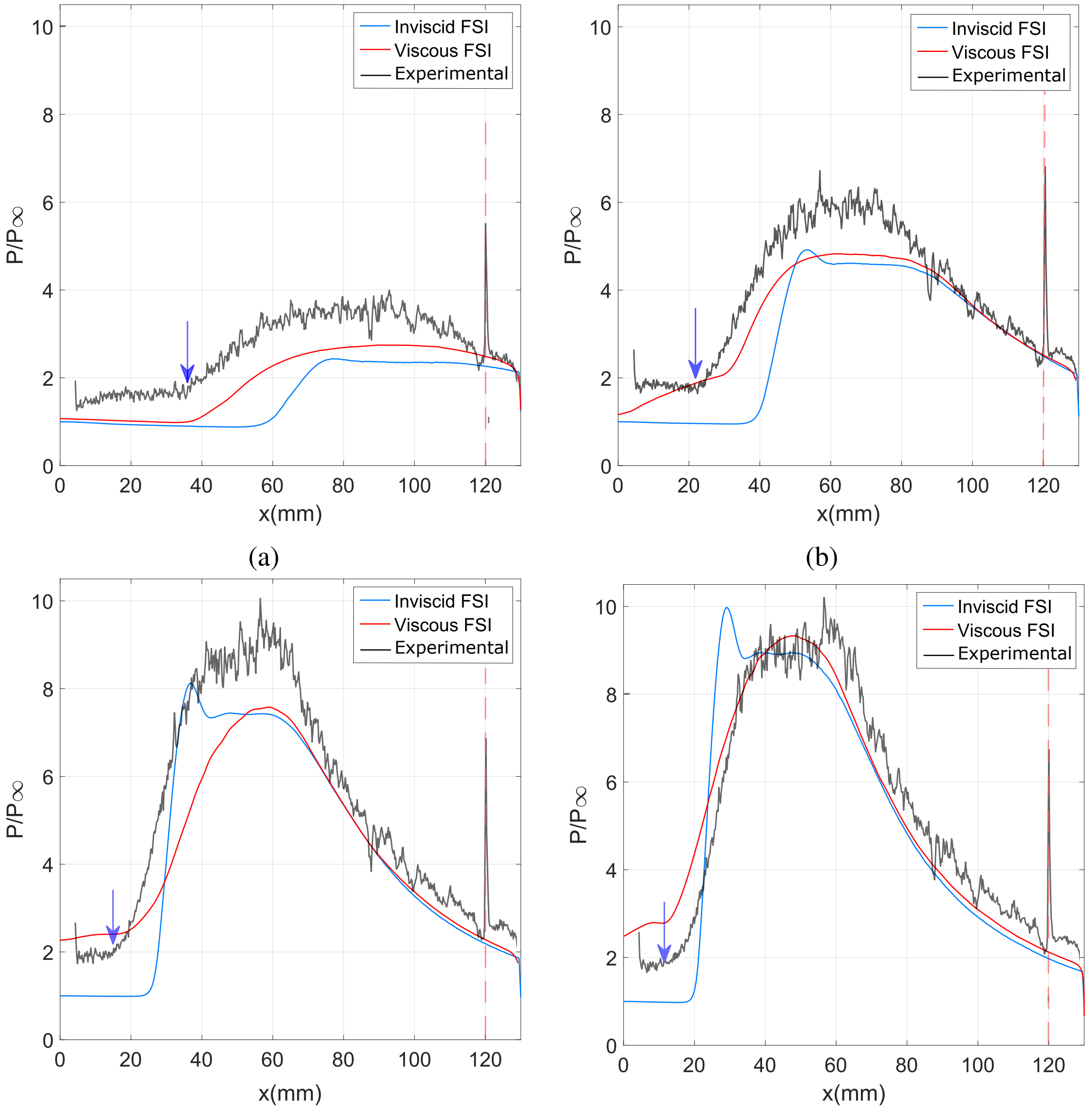

(a) (b)

(c) (d)

Figure 5.7: Normalized pressure(P/P_∞) evolution over the cantilever plate. Vertical blue arrow indicates the shock impingement location. Red dashed line indicates the position of static pressure tap (a) t’= 0ms (b) t’= 2ms (c) t’= 4ms (d) t’= 6ms

5.3.2. Peak Pressure Evolution

5.3.2.1 HFM

In figure 5.8, peak pressure over the surface of the cantilever plate of Inviscid, Viscous simulations in a given instant of time normalized with free stream pressure is plotted against time. In inviscid case, we can clearly see the peak pressure ratio($P_{peak}/P\infty$) oscillates between 10.31 and 1 while in viscous case it oscillates between in 9.5 and 1.24 . In viscous case, however the peak pressure is upper peaks is slightly less this is because the peak pressure in inviscid case is taken from the overshoot caused due to numerical diffusion which can also be seen in figure 5.7. While the dips in peak pressure evolution graph the viscous result is higher this is simply because there is less numerical diffusion at shock waves and thus less pressure overshoot in inviscid results.

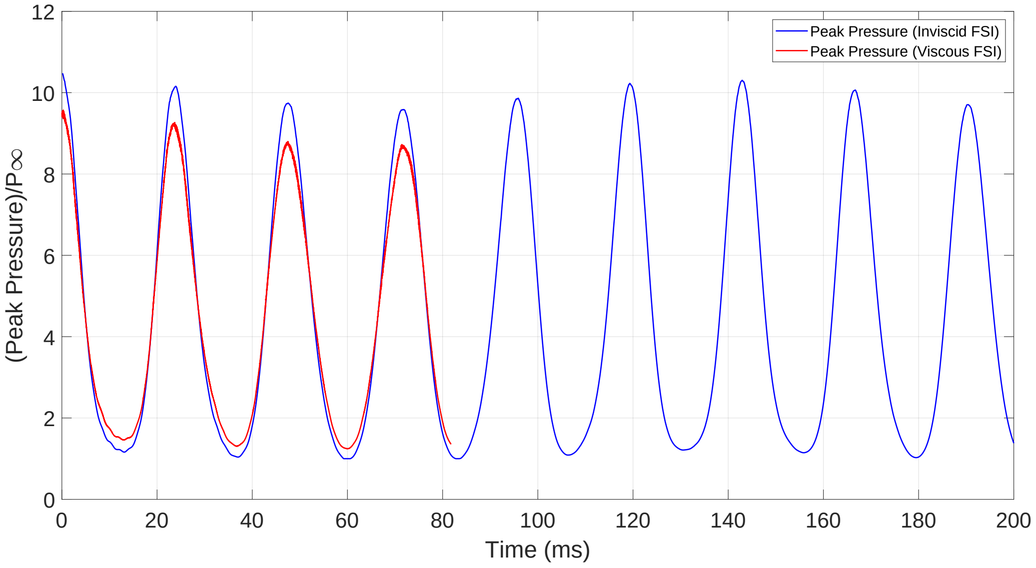

Figure 5.8: Normalized peak pressure evolution on the cantilever plate over time (HFM)

5.3.2.2 LFM

Peak pressure evolution from the low fidelity model is shown in figure 5.9. The maximum normalized peak pressure is found to be about 9.82 from the model using shock expansion and piston theory, and 9.43 from the model using CFD enriched piston theory.

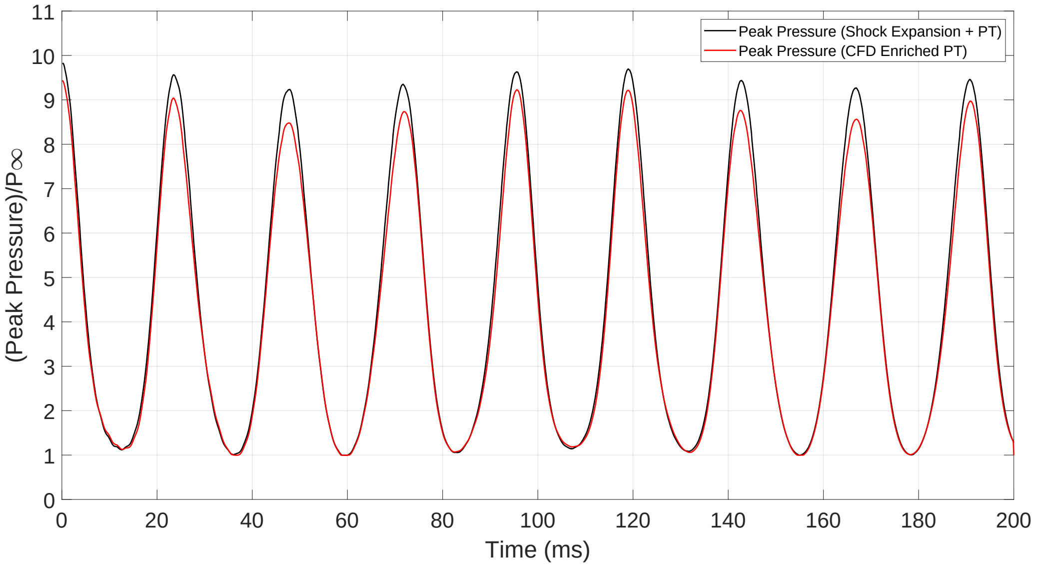

Figure 5.9: Normalized peak pressure evolution on the cantilever plate over time (LFM)

5.3.2.3 Comparision between LFM and HFM

Peak pressure evolution obtained in LFM is compared with the ones obtained in HFM in figure 5.10. The observed discrepancy may be due to the fact that pressure distribution used in LFM was the pressure distribution on the rigid plate and not on the updated geometry of the plate. It can also be observed that peak pressure evolution obtained from the LFM is also modulated by a signal close to 10 Hz, which is consistent with the result obtained in inviscid and viscous simulations.

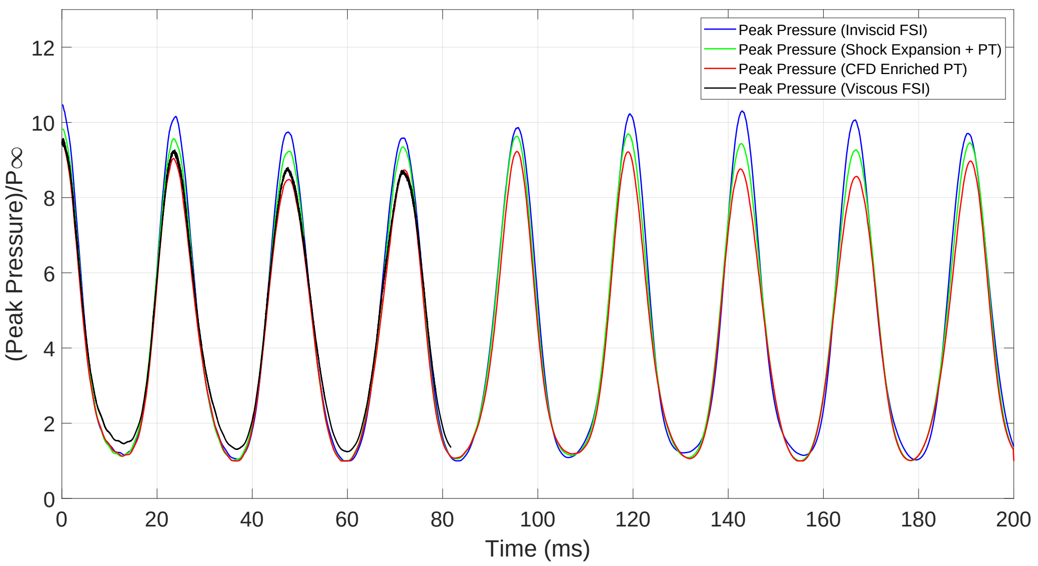

Figure 5.10: Comparison of normalized peak pressure evolution on the cantilever plate over time between LFM and HFM

Power spectra of the peak pressure oscillations in figure 5.11 on the cantilever plate shows two distinct frequency at 42 Hz corresponding to wedge oscillation frequency and smaller peak at 85 Hz that is close to the natural frequency of the plate. Thus, the peak pressure evolution is mainly dominated by oscillations of the wedge. Spectral peaks matches perfectly in all the cases.

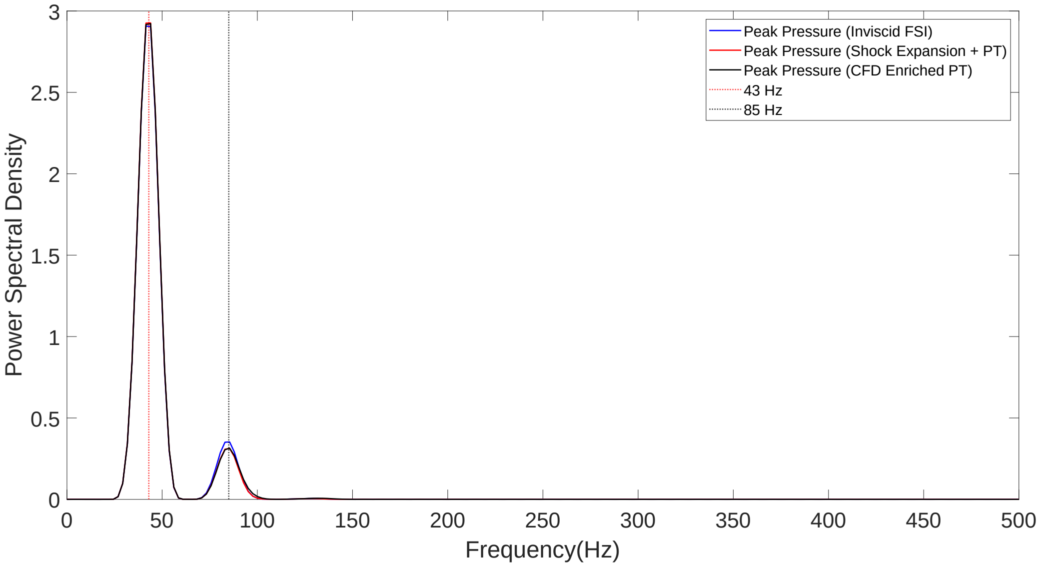

Figure 5.11: Power spectral density of peak pressure evolution over time

5.3.3. Point Pressure Measurement

Time series normalized pressure measurement is taken at the midpoint width wise and 10 mm upstream of the trailing edge of the cantilever plate using pressure transducer in the experiment [7]. The data is compared with the time series pressure data obtained at the same point in the numerical simulation in figure 5.12.

In figure 5.13, phase difference between experimental and numerical simulation due to time taken time taken for flow onset in the experiment is compensated. The trend in numerical simulations is consistent with experimental result with two peak and a dip trend. Peak to trough oscillation of experimental result seems to be damped with time, this corresponds with the damped oscillation of the shock generator. However in viscous and inviscid results peak to trough oscillation is almost constant with time, this can attributed to constant amplitude oscillation of shock generator.

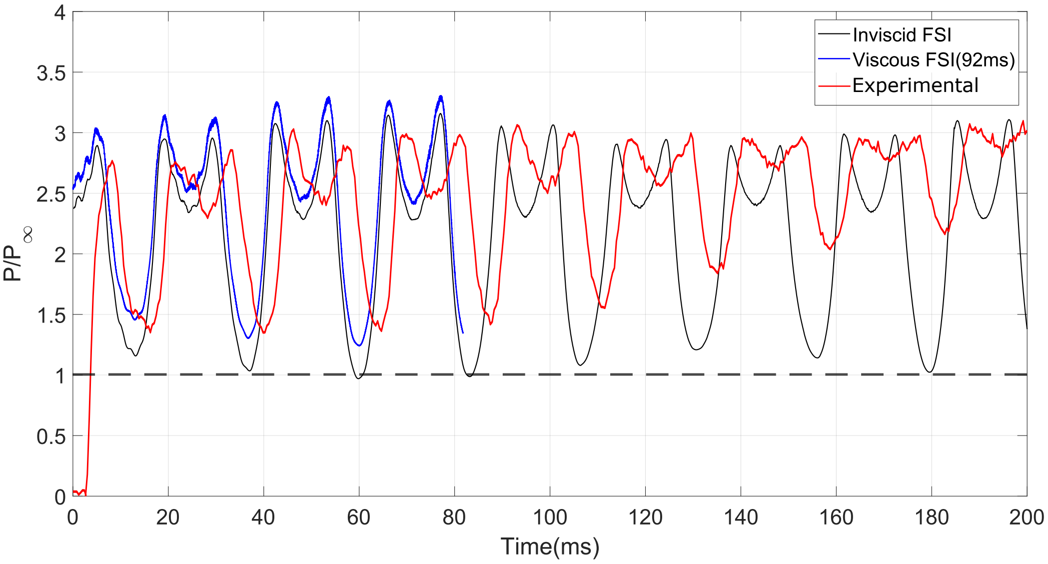

Figure 5.12: Comparison of time series normalized point pressure measurement

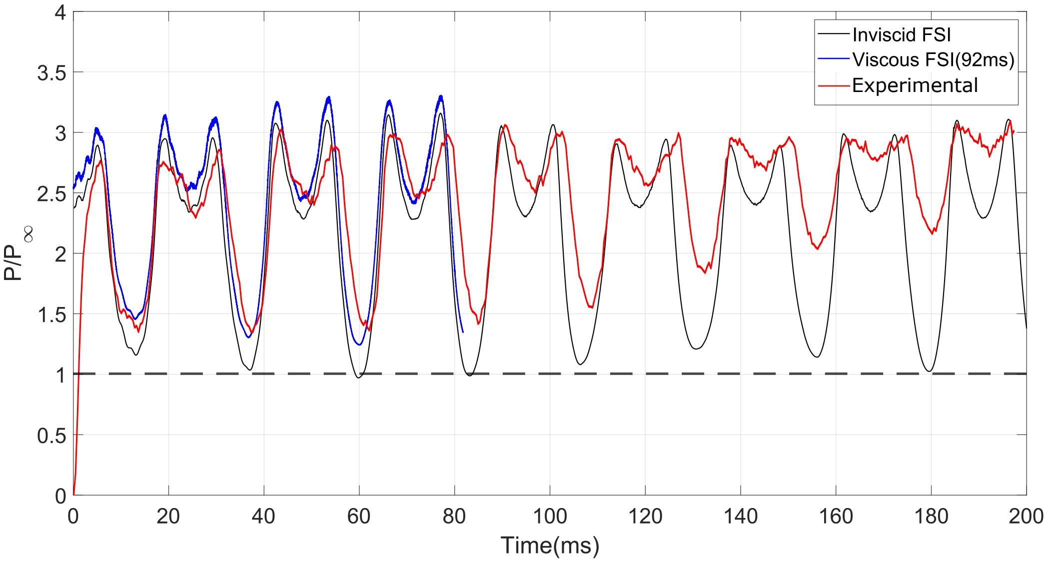

Figure 5.13: Comparison of time series normalized point pressure measurement with phase compensation

5.4. Displacement Based Analysis

5.4.1. HFM

Displacement of upper tip of the cantilever plate obtained during inviscid FSI simulation for 200 ms and viscous FSI for 92 ms is shown in figure 5.14. The maximum positive trailing edge displacement is nearly 2mm and negative trailing edge displacement is 3.01 mm on the first cycle in Inviscid FSI. In Viscous FSI, the max negative displacement in the first cycle is 3.15 mm which very close to 3.21 mm in experiments. In figure 5.15, trailing edge displacement obtained by inviscid FSI and viscous FSI (92 ms) is compared with the experimental trailing edge displacement history [7]. The experimental data was obtained using Laser Profilometer. The mismatch in displacement profile in simulation could be attributed to the difference in induced oscillatory motion of wedge at 42 Hz and actual oscillation profile of wedge as shown in figure 4.12.

We can clearly see the displacement profile is superimposition of multiple frequencies with phase lag which is more evident on the power spectra of trailing edge displacement as shown in figure 5.16. In the power spectra, two distinct peaks at 42 Hz and 90 Hz can be seen which correspond to spectral peaks observed in PSD of experimental results as well.

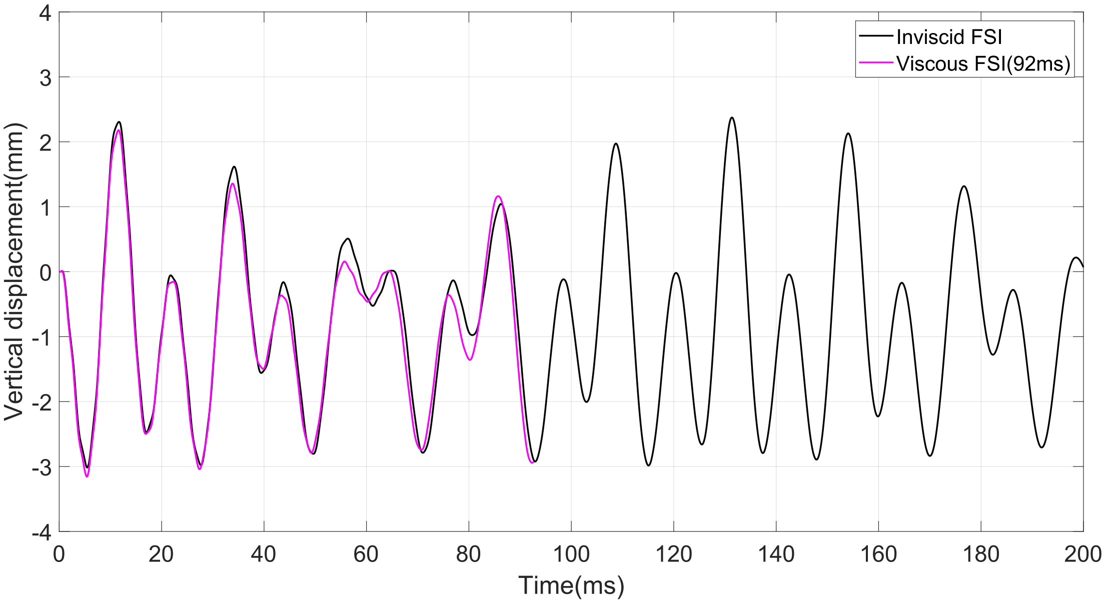

Figure 5.14: Trailing edge displacement profile of the cantilever plate (HFM)

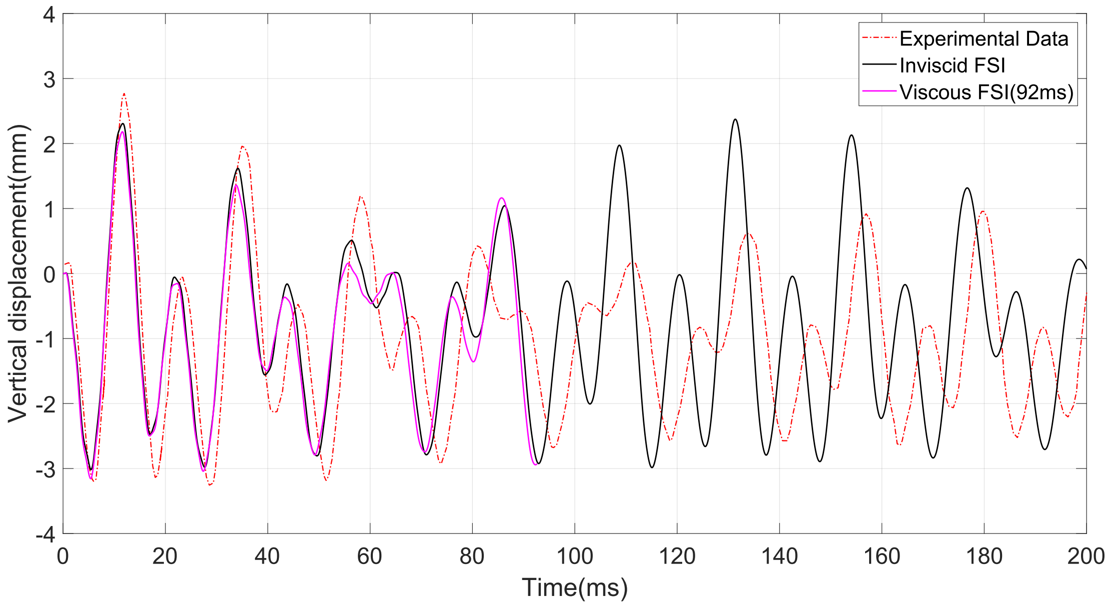

Figure 5.15: Comparison of TE displacement of inviscid and viscous FSI with experimental data

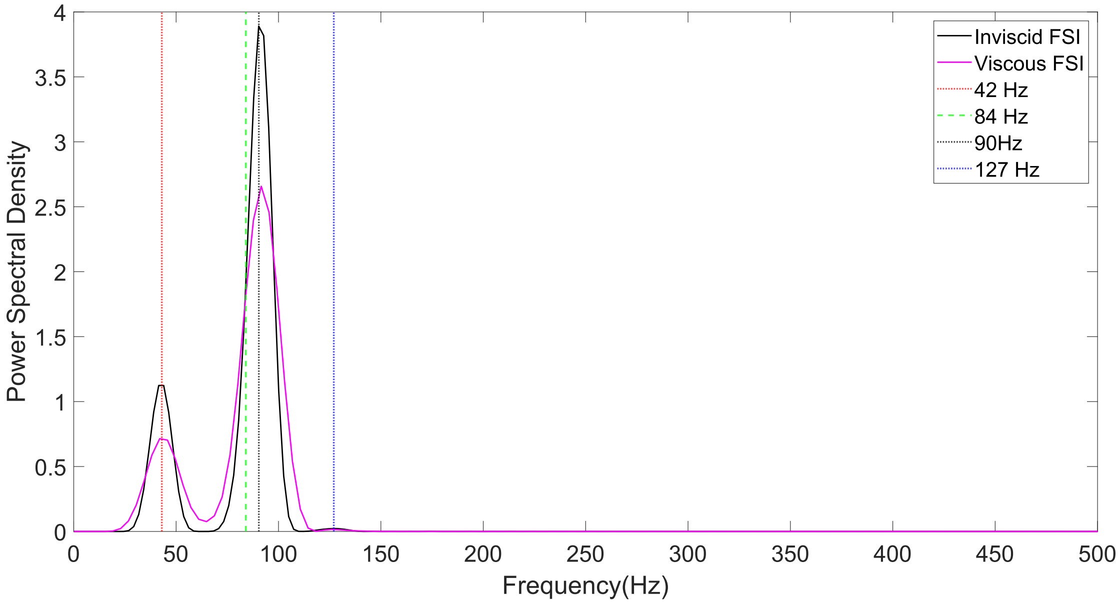

Figure 5.16: Power Spectral Density (PSD) of trailing edge displacement.

5.4.2. LFM (Shock Expansion and Piston Theory)

In this model, the displacement profile of trailing edge of the plate was obtained by feeding pressure from shock expansion theory to piston theory based on plate deflection. The maximum downward displacement of plate tip is found to be about 2.5 mm and the maximum upward displacement of plate tip is found to be about 1.5 mm both of which occurs in first oscillation of plate. The comparison of the displacement profile with the one obtained via inviscid FSI is shown in figure 5.17. The two results are in close agreement with slightly higher frequency in displacement profile calculated using shock expansion and piston theory. This discrepancy may be attributed to difference in the pressure distribution obtained from shock expansion theory which was applied on a rigid plate and not on the updated geometry after displacement. Additionally, inherent errors in the mathematical models used to solve ordinary differential equations (ODEs) could contribute to this divergence.

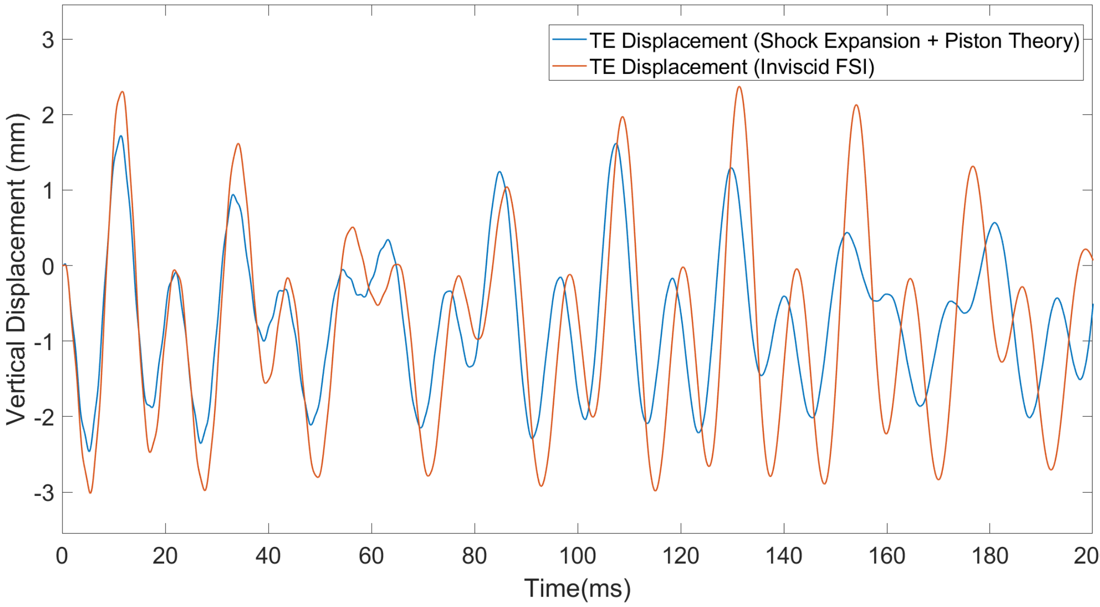

Figure 5.17: Comparison of trailing edge displacement obtained from inviscid FSI and Shock expansion based piston theory

Additionally, FFT was performed on the trailing edge displacement, with results depicted in Figure 5.18. Two dominant frequencies were identified at 42 Hz and 92.7 Hz which is in agreement with the 2 peaks of 42 Hz and 90 Hz, obtained in inviscid FSI. The lower frequency closely matches the oscillating frequency of the shock generator (42 Hz), while the second frequency is near the natural frequency of the first mode of the cantilever plate (89.99 Hz). The power spectral density indicates that the natural frequency of the plate is more dominant in trailing edge displacement, although the oscillating frequency of the shock generator also plays a significant role.

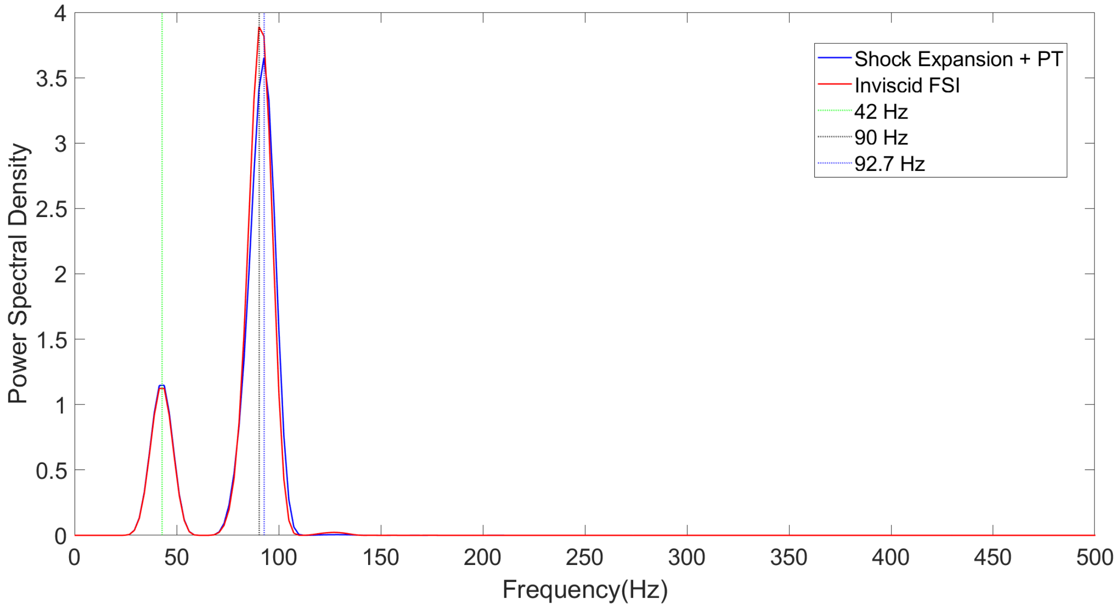

Figure 5.18: Power spectral density of trailing edge displacement obtained from LFM(shock expansion + piston theory)

5.4.3. LFM (CFD Enriched Piston Theory)

In this model, the pressure distribution obtained over plate by numerical simulation was fed into existing LFM model to improve the accuracy of the model. The traling edge diplacement of plate tip was obtained and compared to the result obtained in inviscid FSI as shown in figure 5.19. The maximum downward displacement of plate tip is found to be about 3 mm and the maximum upward displacement of plate tip is found to be about 2 mm both of which occurred in first oscillation of plate. The two results are in close agreement up to $t = 95$ ms, after which amplitude and phase difference emerges which may be accounted by the fact that the frequency of two displacement are slightly off due to which the error accumulates as time increases. It can be further demonstrated by the result of FFT carried out in displacement of plate tip as shown in figure 5.20. We can observe two dominant peaks at f = 42 Hz and f = 92.7 Hz which is close to the peaks obtained in inviscid FSI (f =42 Hz and f =90 Hz).

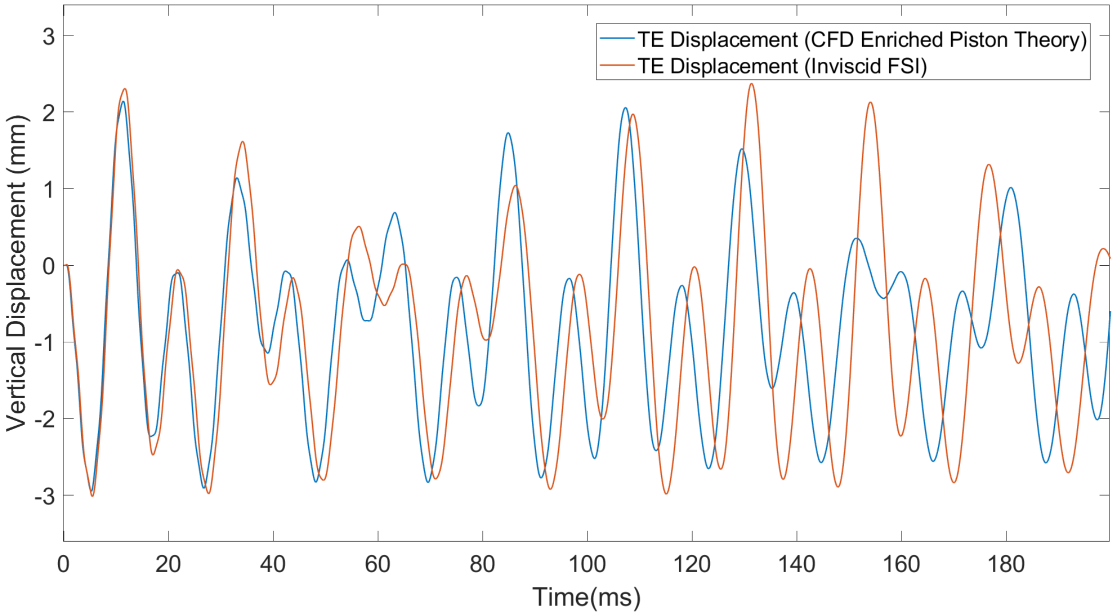

Figure 5.19: Comparison of trailing edge displacement obtained from inviscid FSI and CFD enriched piston theory

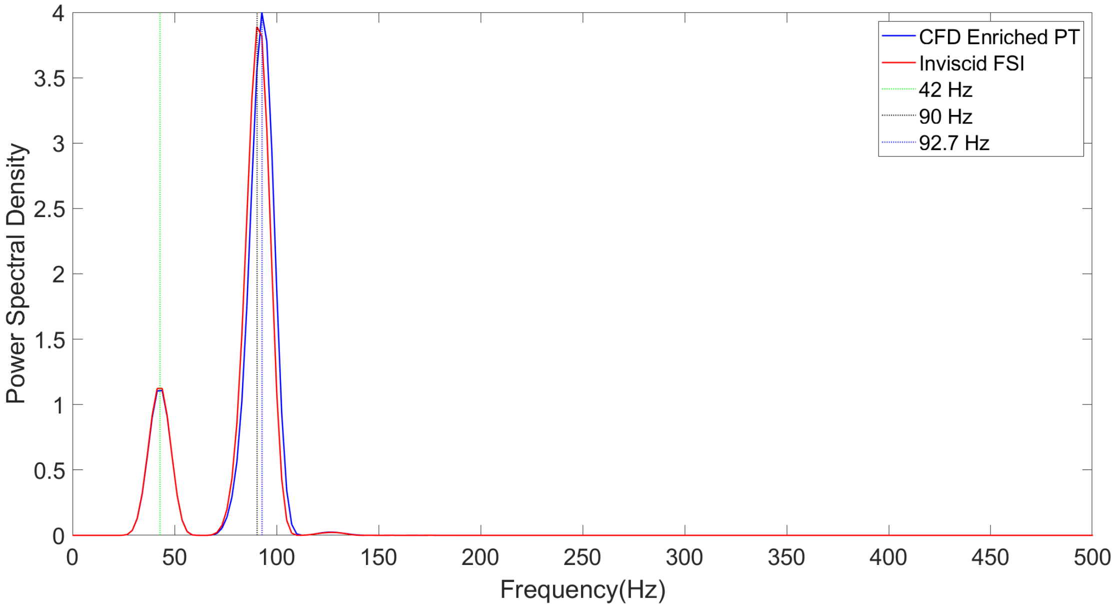

Figure 5.20: Power spectral density of trailing edge displacement obtained from LFM (CFD enriched piston theory)

5.4.4. Analysis of Filtered Displacement

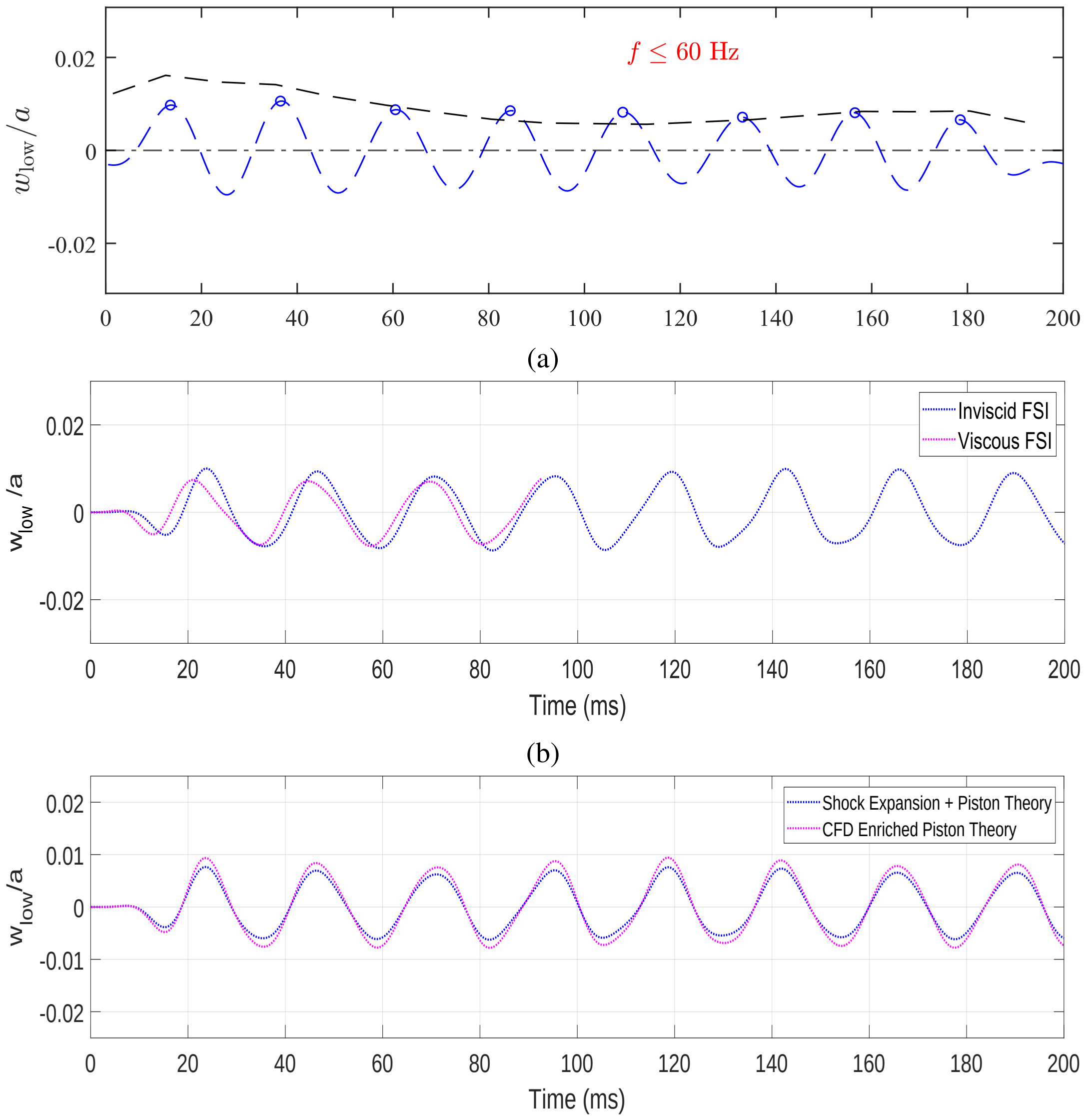

(a)

(b)

(c)

Figure 5.21: Low pass filtered signal (< 60 Hz) of TE displacement (a) Experimental data (b) inviscid and viscous FSI (c) LFM

The displacement signal is filtered using high pass filter and low pass filter using cutoff frequency of 60 Hz which can be justified from the gap between two power spectra peaks at 90 and 42 Hz in figure 5.16. Low pass (< 60 Hz) and high pass (> 60 Hz) filter is applied to the TE displacement signal using Butterworth method. Low pass (< 60 Hz) filtered signal obtained in viscous and inviscid simulations as shown in figure 5.21b and through low fidelity modeling 5.21c, which has frequency of 42 Hz and constant amplitude throughout the test duration of 200ms which is consistent with the experimental data as shown in figure 5.21a.

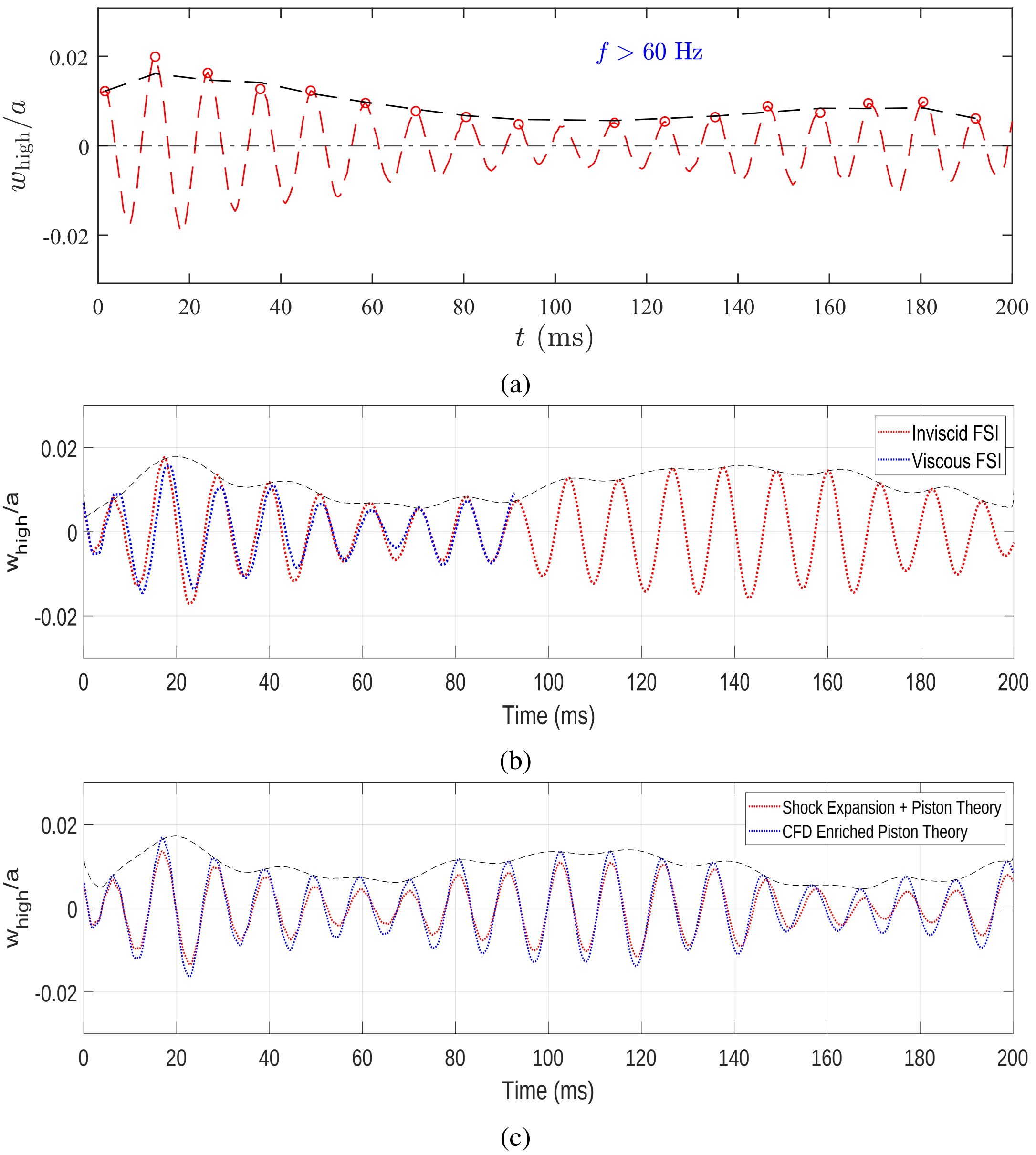

(a)

(b)

(c)

Figure 5.22: High pass filtered signal (> 60 Hz) of TE displacement (a) Experimental data (b) inviscid and viscous FSI (c) HFM

Amplitude of high pass filtered signal of the experimental data is reported to be modulated by highly energetic low frequency (10 Hz) disturbance in freestream [7]. However in inviscid and viscous FSI even with constant freestream condition, amplitude of high pass filtered signal seems to be modulated by frequency ($\approx$10 Hz) which is consistent with the peak pressure evolution with time as shown in figure 5.8. Moreover, same trend is also observed in high pass filtered signal obtained through LFM as shown in figure 5.22c. This shows that the high pass filtered signal is affected by peak pressure fluctuations with time.

Further on the reason why the high pass filtered signal is modulated by a signal close to 10 Hz as shown by the PSD of envelope of high pass filtered signal in figure 5.23. The trend is consistent with peak pressure evolution as well and the reason for such trend is simply because of combination of wedge oscillation and plate oscillation. This is proven by the fact that the shock impingement position when the flow deflection angle is max i.e. 10 degrees is seen to oscillate close to frequency of 10 Hz as shown in figure 5.24. Similarly the superimposition of wedge displacement profile on the trailing edge displacement profile as shown in figure 5.25 gives us the similar trend making the argument even more strong. Cross-correlation was done between peak pressure evolution and trailing edge displacement profile which showed peak around 10 Hz as shown in figure 5.26.

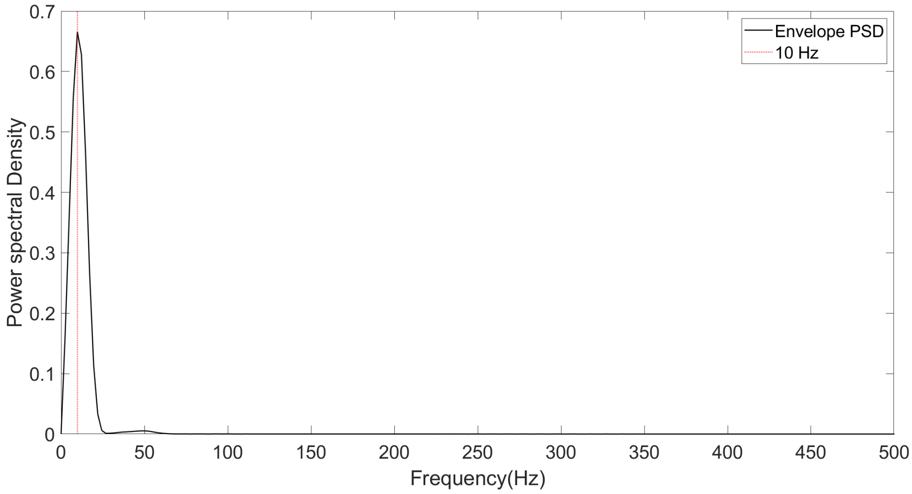

Figure 5.23: Power spectral density of envelope of high pass filtered signal

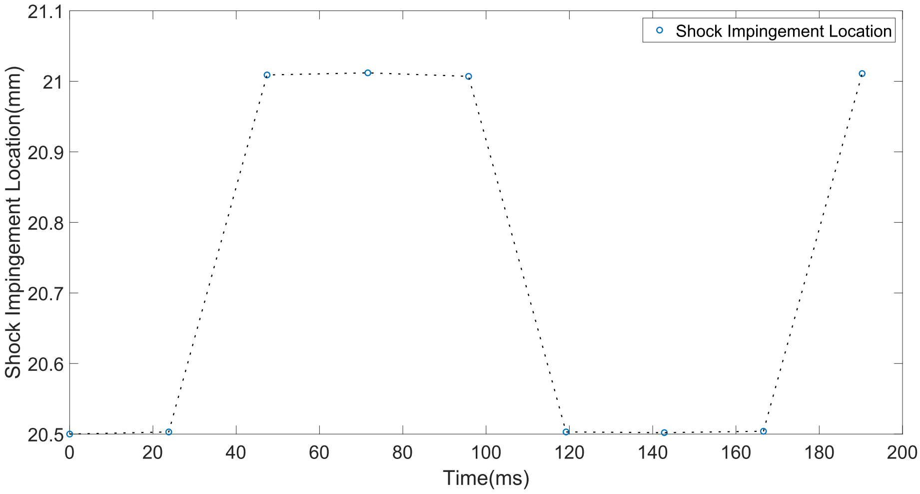

Figure 5.24: Shock impingement location at maximum flow deflection angle with time

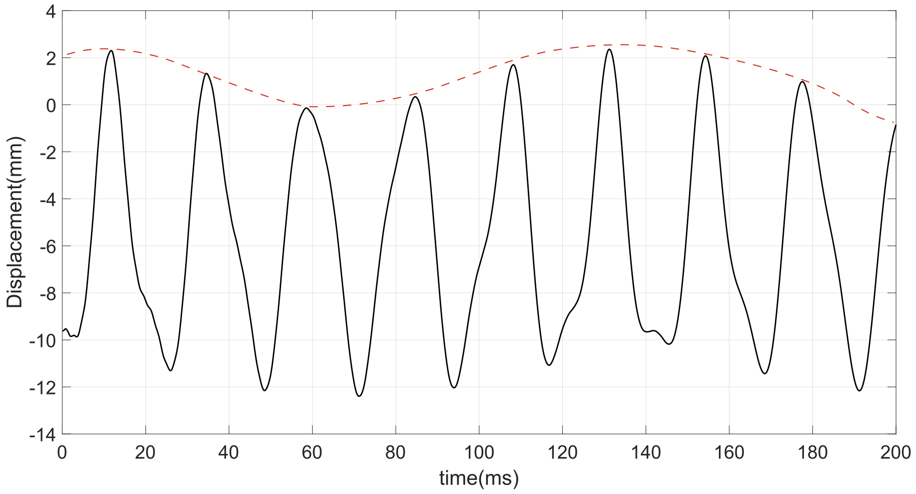

Figure 5.25: Displacement profile of plate superimposed with the wedge motion

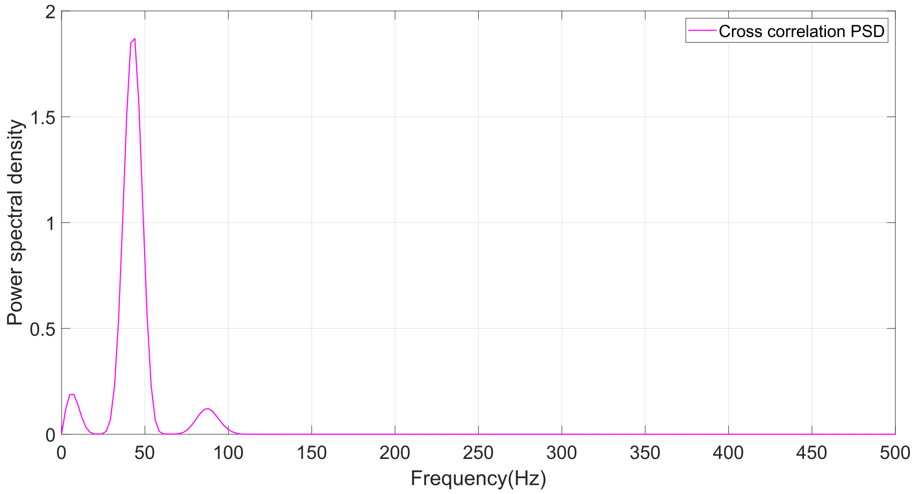

Figure 5.26: Cross correlation PSD between superimposed TE displacement profile and peak pressure evolution

CHAPTER 6: LIMITATIONS, PROBLEMS FACED AND BUDGET ANALYSIS

6.1. Limitations

- Thermal interaction is not considered in this project and thus our simulation results might deviate slightly from experimental results.
- Using a partitioned approach, there is a tradeoff of stability and accuracy to minimize computational cost.
- 2D simulation does not incorporate three-dimensional flow effects. This can create a slight deviation from the experimental results.
- The turbulent behavior of flow is not accounted for in the study.
- While modelling the oscillating nature of the wedge, we could not give a rigid body motion to simulate the FSI of the wedge because preCICE did not support it. Instead we gave sinusoidal oscillating nature to wedge which was different from actual motion of wedge.

6.2. Problems Faced

- The preCICE adapter did not support coupling between the sixDOFRigidBodyMotion solver and Solid CalculiX solver, so we used an induced motion for the wedge.
- Frequent solver crashes were encountered in the viscous simulations due to the grid just above the plate collapsing. This was tackled by lowering the aspect ratio of the grids just above the plate which is not ideal.
- Viscous FSI demanded very high computational resources and the computational resources available constrained us to perform the simulation in a coarse grid.

6.3. Budget Analysis

The computational cost is calculated using Amazon's Web Service (CFD Direct from the Cloud) approximated for a virtual system with configuration of CPU with 16 cores, 32 GB RAM which costs \$0.78 per hour [27]. A computational time of initial testing as well as final simulation is taken into account for the calculation of total computational cost[1]. The total computational cost is tabulated in table 6.1. A SSD of 500 GB was purchased for storage of data. The total budget breakdown is tablated in table 6.2.

Table 6.1: Total Computational Cost

Simulation	**Time (Hpurs)**	**Approximate Cost**
Inviscid	45	Rs. 4635
Grid Convergence	60	Rs. 6180
Viscous	1080 (estimated)	Rs. 111,240
	Total	Rs. 1,22,055

Table 6.2: Budget Breakdown

S.N.	**Particulars**	**Cost**
1	Computational Cost	Rs. 1,22,055
2	Documentation	Rs. 8,000
3	SSD	Rs. 5,000
	Total	Rs. 1,35,055

CHAPTER 7: CONCLUSION AND SCOPE FOR FUTURE ENHANCEMENT

7.1. Conclusion

In conclusion, our study investigates the dynamic behavior of a cantilever plate subjected to the rotatory oscillating motion of a wedge generating periodic shock impingement on the plate. The wedge oscillates at a frequency of 42 Hz, causing corresponding changes in the shock impingement location [28].

Comparing schlieren images and pressure evolution between experimental and numerical results, we observe consistent trends, although the inviscid simulation exhibits downsides such as a downstream shift in shock impingement and absence of separation bubbles. The pressure plateau before shock impingement is slightly greater in experiments due to absence of separation shock in the inviscid simulation and coarse grid in viscous simulation. The power spectra of peak pressure oscillations shows dominant peak at 42 Hz and lower spectral peak at 85 Hz (3.19% lower than natural first mode of oscillation of cantilever plate). The peak pressure value increased by around 4.1% (227.3 Pa) in viscous CFD result when compared to inviscid CFD result at maximum flow deflection angle.

The displacement profile of the cantilever plate from inviscid and viscous Fluid-Structure Interaction (FSI) simulation is compared with experimental data, showing superimposition of multiple frequencies with phase lag. The maximum deflection on the first cycle in Inviscid and Viscous FSI obtained was 3.01 mm and 3.15 mm with error 1.86 % and 6.2 % respectively. The power spectra of trailing edge displacement reveal distinct peaks at 42 Hz and 90 Hz which is consistent with PSD of experimental TE displacement profile. Filtering the displacement signal using low pass ($<$ 60 Hz) and high pass ($>$ 60 Hz) methods demonstrates consistency with experimental data. The 10 Hz amplitude modulation of high pass filtered signal was found to be due to combination of wedge oscillation and cantilever plate in both inviscid, viscous FSI as well as in LFM cases.

Shock Expansion based Piston theory was validated with pressure evolution obtained over the cantilever plate in inviscid simulation. Power spectra of TE displacement profile obtained using SE based PT and CFD enriched PT showed two spectral peaks at 42

Hz and 92.7 Hz (3% greater than experimental spectral peak). The max displacement for the first peak of the trailing edge displacement profile is found to be 2.46 mm using shock Expansion based Piston theory whereas the inviscid FSI solution predicted it to be 3.01 mm. Similarly, CFD enriched Piston Theory predicted it to be 2.94 mm which is more consistent to the result from inviscid simulation result. A compiled comparison of data is presented in the table 7.1.

Table 7.1: Compiled comparison of data

Data From	TE Displacement (1st cycle)	Displacement peak (major, minor)	Pressure peak (major, minor)
Experiment	-3.21 mm	90 Hz, 42 Hz	N/A
Viscous FSI	-3.15 mm	90 Hz, 42 Hz	42 Hz, 84 Hz
Inviscid FSI	-3.01 mm	90 Hz, 42 Hz	42 Hz, 84 Hz
SE + PT	-2.46 mm	92.7 Hz, 42 Hz	42 Hz, 85 Hz
CFD + PT	-2.94 mm	92.7 Hz, 42 Hz	42 Hz, 85 Hz

7.2. Scope For Future Enhancement

- Instead of supplying an induced motion to the wedge, it can be allowed to oscillate with its natural frequency with the flow to better match the experimental conditions. This is currently not available to do via the preCICE adapter so a different adapter to couple the fluid and solid maybe required.
- This numerical simulation was carried out entirely for laminar flow field. However, since the hypersonic flow is bound to undergo transition in cases of SWBLI, a fully coupled turbulent FSI simulation of this case and the comparison of its results with the experimental and the laminar simulation results is recommended.
- There will be significant thermal interactions if the wall is at a higher temperature. So thermal effects can be considered and a fully coupled Fluid Thermal Structure Interaction simulation can be performed in the future.

References

[1] N. Poudel, S. Sahani, and S. Pudasaini, “Numerical study of hypersonic fluid structure interaction on a cantilevered plate with shock impingement,” Ph.D. dissertation, IOE Pulchowk, 2023.

[2] Y. Bazilevs, K. Takizawa, and T. E. Tezduyar, *Computational fluid-structure interaction: methods and applications*. John Wiley & Sons, 2013.

[3] “North American X-15A-2 — nationalmuseum.af.mil,” https://www.nationalmuseum.af.mil/Visit/Museum-Exhibits/Fact-Sheets/Display/Article/195761/north-american-x-15a-2/, [Accessed 04-01-2024].

[4] G. Currao, “Experimental study of hypersonic fluid structure interaction with shock impingement on a cantilevered plate,” Ph.D. dissertation, UNSW Sydney, 2018.

[5] E. H. Hirschel and C. Weiland, *Selected aerothermodynamic design problems of hypersonic flight vehicles*. Springer Science & Business Media, 2009, vol. 229.

[6] G. M. Currao, L. P. McQuellin, A. J. Neely, F. Zander, D. Buttsworth, J. J. McNamara, and I. Jahn, “Oscillating shock impinging on a flat plate at mach 6,” in *AIAA Aviation 2019 Forum*, 2019, p. 3077.

[7] M. K. Talluru, L. P. McQuellin, and A. J. Neely, “Oscillating shock wave boundary layer interactions on a cantilever plate,” in *25th AIAA International Space Planes and Hypersonic Systems and Technologies Conference*, 2023, p. 3094.

[8] J. D. Anderson, *Hypersonic and high temperature gas dynamics*. Aiaa, 1989.

[9] B. Thuruthimattam, P. Friedmann, K. Powell, and J. McNamara, “Aeroelasticity of a generic hypersonic vehicle,” in *43rd AIAA/ASME/ASCE/AHS/ASC Structures, Structural Dynamics, and Materials Conference*, 2002, p. 1209.

[10] G. Hou, J. Wang, and A. Layton, “Numerical methods for fluid-structure interaction—a review,” *Communications in Computational Physics*, vol. 12, no. 2, pp. 337–377, 2012.

[11] M. S. Holden, “Shock wave-turbulent boundary layer interaction in hypersonic flow,” in *10th Aerospace Sciences Meeting*, 1977, p. 74.

[12] L. TRILLING, “Oscillating shock boundary-layer interaction,” *Journal of the Aerospace Sciences*, vol. 25, no. 5, pp. 301–304, 1958.

[13] V. Pasquariello, S. Hickel, and N. A. Adams, “Unsteady effects of strong shock-wave/boundary-layer interaction at high reynolds number,” *Journal of Fluid Mechanics*, vol. 823, pp. 617–657, 2017.

[14] G. M. Currao, L. P. McQuellin, A. J. Neely, S. L. Gai, S. O’Byrne, F. Zander, D. R. Buttsworth, J. J. McNamara, and I. Jahn, “Hypersonic oscillating shock-wave/boundary-layer interaction on a flat plate,” *AIAA journal*, vol. 59, no. 3, pp. 940–959, 2021.

[15] J. J. McNamara, A. R. Crowell, P. P. Friedmann, B. Glaz, and A. Gogulapati, “Approximate modeling of unsteady aerodynamics for hypersonic aeroelasticity,” *Journal of Aircraft*, vol. 47, no. 6, pp. 1932–1945, 2010.

[16] S. Bhattrai, L. McQuellin, G. M. Currao, A. Neely, and D. Buttsworth, “Influence of hypersonic fluid-structure interaction on the control authority of a trailing-edge flap,” in *22nd AIAA International Space Planes and Hypersonics Systems and Technologies Conference*, 2018, p. 5265.

[17] G. M. Currao, A. J. Neely, C. M. Kennell, S. L. Gai, and D. R. Buttsworth, “Hypersonic fluid–structure interaction on a cantilevered plate with shock impingement,” *AIAA journal*, 2019.

[18] P. B. Vasconcelos, L. P. McQuellin, T. Krishna, and A. Neely, “Experimental study of hypersonic fluid-structure interactions on an inclined clamped-free-clamped-free compliant panel,” in *ASCEND 2021*, 2021, p. 4232.

[19] Anderson, *Fundamentals of Aerodynamics, 6th Edition*. Mc Graw Hill Education, 2017.

[20] A. P. Boresi and R. J. Schmidt, *Advanced mechanics of materials*. John Wiley & Sons, 2002.

[21] K. T. Y. Bazilecs and T. E. Tezduyar, *Computational fluid-structure interaction: methods and applications*. John Wiley & Sons, 2013.

[22] H.-J. Bungartz, F. Lindner, B. Gatzhammer, M. Mehl, K. Scheufele, A. Shukaev, , and B. Uekermann, “Precice-a fully parallel library for multi-physics surface coupling,” *Computer & Fluids*, vol. 141, pp. 250–258, 2016.

[23] B. Birch, D. Buttsworth, and F. Zander, “Measurements of freestream density fluctuations in a hypersonic wind tunnel,” *Experiments in Fluids*, vol. 61, no. 7, p. 158, 2020.

[24] J. J. McNamara and P. P. Friedmann, “Aeroelastic and aerothermoelastic analysis in hypersonic flow: past, present, and future,” *AIAA journal*, vol. 49, no. 6, pp. 1089–1122, 2011.

[25] A. S. of Mechanical Engineers. Fluids Engineering Division, *Quantification of Uncertainty in Computational Fluid Dynamics*. American Society of Mechanical Engineers, 1993.

[26] G. J. Leishman, *Principles of helicopter aerodynamics with CD extra*. Cambridge university press, 2006.

[27] AWS, “Cfd direct from the cloud,” https://aws.amazon.com/marketplace/pp/prodview-ojxm4wfrodtj4?sr=0-1&ref_=beagle&applicationId=AWSMPContessa#pdp-pricing, accessed: 2023.06.01.

[28] G. Z. H. Ashley, “Piston theory-a new aerodynamic tool for the aeroelastician,” *Journal of the aeronautical sciences*, vol. 23, no. 12, pp. 1109–1118, 1956.